JCB Journal of Cell Biology

ARTICLE

Atg9 establishes Atg2-dependent contact sites between the endoplasmic reticulum and phagophores

Rubén Gómez-Sánchez[1*], Jaqueline Rose[3*], Rodrigo Guimarães[1,2**], Muriel Mari[1**], Daniel Papinski[4], Ester Rieter[2], Willie J. Geerts[5], Ralph Hardenberg[1], Claudine Kraft[4,6], Christian Ungermann[3], and Fulvio Reggiori[1,2]

The autophagy-related (Atg) proteins play a key role in the formation of autophagosomes, the hallmark of autophagy. The function of the cluster composed by Atg2, Atg18, and transmembrane Atg9 is completely unknown despite their importance in autophagy. In this study, we provide insights into the molecular role of these proteins by identifying and characterizing Atg2 point mutants impaired in Atg9 binding. We show that Atg2 associates to autophagosomal membranes through lipid binding and independently from Atg9. Its interaction with Atg9, however, is key for Atg2 confinement to the growing phagophore extremities and subsequent association of Atg18. Assembly of the Atg9–Atg2–Atg18 complex is important to establish phagophore–endoplasmic reticulum (ER) contact sites. In turn, disruption of the Atg2–Atg9 interaction leads to an aberrant topological distribution of both Atg2 and ER contact sites on forming phagophores, which severely impairs autophagy. Altogether, our data shed light in the interrelationship between Atg9, Atg2, and Atg18 and highlight the possible functional relevance of the phagophore–ER contact sites in phagophore expansion.

Introduction

Autophagy is an evolutionarily conserved cellular transport pathway in which cytoplasmic components including protein aggregates and damaged or superfluous organelles are targeted for turnover within the yeast and plant vacuole or the mammalian lysosome (Nakatogawa et al., 2009; Mizushima et al., 2011; Kraft and Martens, 2012; Lamb et al., 2013). The resulting degradation products are then reused as building blocks to generate new macromolecules or as a source of energy. The hallmark of autophagy is the sequestration of the structures targeted to degradation by large double-membraned vesicles called autophagosomes, which are ultimately responsible to deliver their content into the vacuole/lysosome (Nakatogawa et al., 2009; Mizushima et al., 2011; Kraft and Martens, 2012; Lamb et al., 2013).

So far, 41 autophagy-related (*ATG*) genes have been identified, several of which are also found in higher eukaryotes. 16 of them belong to the core Atg machinery as they are highly conserved across eukaryotes (Nakatogawa et al., 2009; Mizushima et al., 2011; Kraft and Martens, 2012; Lamb et al., 2013). They are essential for the formation and expansion of the phagophore, which forms at the phagophore assembly site (PAS) and matures into an autophagosome (Suzuki et al., 2007; Nakatogawa et al., 2009; Mizushima et al., 2011; Kraft and Martens, 2012; Lamb et al., 2013). The origin of the membranes required for both the phagophore nucleation and its expansion still remains largely elusive. The ER appears to play a central role as the extremities of phagophores are associated with this subcellular compartment (Graef et al., 2013; Suzuki et al., 2013), and mammalian autophagosomes form in specialized subdomains of the ER known as omegasomes (Axe et al., 2008; Hayashi-Nishino et al., 2009; Ylä-Anttila et al., 2009; Uemura et al., 2014). To shed light on the question about the source of autophagosomal membranes, several studies have focused on Atg9, the only transmembrane protein within the core Atg machinery (Lang et al., 2000; Noda et al., 2000; Young et al., 2006). Although most Atg proteins are cytoplasmic and associate with the forming autophagosome upon autophagy induction, yeast Atg9 is found in multiple punctuate structures within

[1]Department of Cell Biology, University of Groningen, University Medical Center Groningen, Groningen, Netherlands; [2]Department of Cell Biology, University Medical Center Utrecht, Utrecht University, Utrecht, Netherlands; [3]Department of Biology/Chemistry, Biochemistry Section, University of Osnabrück, Osnabrück, Germany; [4]Max F. Perutz Laboratories, University of Vienna, Vienna Biocenter, Vienna, Austria; [5]Biomolecular Imaging, Bijvoet Center, Utrecht University, Utrecht, Netherlands; [6]Institute of Biochemistry and Molecular Biology, Institute of Molecular Medicine and Cell Research, Faculty of Medicine, University of Freiburg, Freiburg, Germany.

*R. Gómez-Sánchez and J. Rose contributed equally to this paper; **R. Guimarães and M. Mari contributed equally to this paper; Correspondence to Fulvio Reggiori: f.m.reggiori@umcg.nl; Christian Ungermann: cu@uos.de.

cells, also known as Atg9 reservoirs (Reggiori et al., 2004; Mari et al., 2010; Ohashi and Munro, 2010; Yamamoto et al., 2012). Atg9 cycles between these reservoirs and the PAS, and at least one of the Atg9 reservoirs provides membranes required for the generation of the PAS by relocalizing in close proximity of vacuoles (Mari et al., 2010; Yamamoto et al., 2012). ATG9A, the mammalian orthologue of Atg9, exhibits a similar dynamic behavior by trafficking between the trans-Golgi network, endosomes, and plasma membrane and also forming autophagosomes (Young et al., 2006; Takahashi et al., 2011; Longatti et al., 2012; Orsi et al., 2012; Puri et al., 2013).

Atg2 is a large and conserved core Atg protein of ∼200 kD. It is essential for autophagosome biogenesis, and its association to the PAS requires several factors including Atg9 and phosphatidylinositol-3-phosphate (PtdIns3P; Barth and Thumm, 2001; Shintani et al., 2001; Wang et al., 2001; Rieter et al., 2012). Atg2 forms a complex with Atg18 (Suzuki et al., 2007; Obara et al., 2008; Rieter et al., 2012), a protein that directly binds PtdIns3P and localizes to the PAS but also to endosomes and vacuoles (Guan et al., 2001; Dove et al., 2004; Krick et al., 2008; Obara et al., 2008). So far, it is not yet clear whether Atg2 and Atg18 are recruited sequentially or as a complex to the PAS (Obara et al., 2008; Rieter et al., 2012). Because almost all the Atg core proteins are present on the autophagosomal intermediates, which accumulate in the *atg2Δ* knockout strain, it has been hypothesized that the Atg2–Atg18 complex could operate just before or when an autophagosome is completed, potentially also in Atg9 recycling (Reggiori et al., 2004; Reggiori and Ungermann, 2017). Importantly, Atg2 and Atg18 are conserved across species. *Caenorhabditis elegans* harbors an equivalent complex composed by ATG-2 and EPG-6, which also regulates ATG-9 trafficking (Lu et al., 2011). Similarly, mammalian cells possess two redundant homologues, i.e., ATG2A and ATG2B, which form a complex with WIPI4, one of the four human counterparts of Atg18, and are involved in maintaining the correct ATG9A subcellular distribution (Velikkakath et al., 2012; Bakula et al., 2017; Zheng et al., 2017).

To unveil the role of the interplay between Atg2, Atg18, and Atg9 and to assign a molecular function to Atg2, we searched for the interaction site between Atg2 and Atg9. Our study of the corresponding Atg9-binding mutants of Atg2 now reveals that Atg9 is required for Atg2 localization to the extremities of the phagophore, where the association with the ER appears to take place. Although not precluding recruitment to the PAS, disruption of Atg2 binding to Atg9 leads to both Atg2 distribution and ER tethering along the entire phagophore surface. This reveals that Atg2 has an intrinsic ability to bind to the ER. Collectively, our data show that Atg9 interaction confines Atg2 to the extremities of the expanding phagophore, a likely prerequisite for both a productive association with the ER and efficient autophagosome biogenesis.

Results

Atg2 directly interacts with Atg9

To test the interaction between Atg2 and Atg9, we exploited the yeast two-hybrid (Y2H) system (James et al., 1996). The plasmid expressing a fusion between the Gal4 activation domain (AD) and Atg9 was cotransformed into the Y2H test strain together with an empty vector or a plasmid carrying either Atg2 or Atg18 tagged with the Gal4 DNA binding domain (BD). No growth was observed in the negative control, whereas cells expressing both BD-Atg2 and AD-Atg9 grew, showing that Atg2 and Atg9 interact (Fig. 1 A). When Atg18 was deleted in this strain background, growth was maintained, indicating that Atg18 is dispensable for the binding between Atg2 and Atg9. Importantly, absence of growth suggested that Atg9 and Atg18 do not directly interact.

Next, we turned to the split-ubiquitin system to validate these results. This technique is often used to study interactions involving transmembrane proteins (Wittke et al., 1999). Moreover, it allows the analysis of interactions at the site where those take place. To this end, Atg2, Atg9, and Atg18 were N-terminally fused with the N-terminal fragment of ubiquitin (N_{ub}), whereas Atg9 was C-terminally tagged with the C-terminal fragment of ubiquitin (C_{ub}). The plasmids carrying the different constructs were then cotransformed into either a WT or an *atg2Δ* strain to test protein interaction. The empty plasmids were used as the negative control, and as expected, cells carrying these constructs were able to grow on the test plate, which opposite to the Y2H assay, indicates no interaction (Fig. 1 B). Self-interaction of Atg9 (Reggiori et al., 2005; He et al., 2008) was used as a positive control. Importantly, cells simultaneously expressing Atg9-C_{ub} and N_{ub}-Atg2 were also not able to grow, confirming that Atg9 binds to Atg2 (Fig. 1 B). Very interestingly, interaction between Atg9-C_{ub} and N_{ub}-Atg18 was detected in WT cells but not in *atg2Δ* cells.

Loss of Atg2 affects the interaction between Atg9 and Atg18 (Fig. 1 B; Reggiori et al., 2004). To determine whether Atg18 is required for the interaction of Atg2 and Atg9, we coimmunoprecipitated Atg2–tandem affinity purification (TAP) from WT and *atg18Δ* cells and analyzed for Atg9 binding. Atg9 was efficiently coisolated with Atg2 in the presence or absence of Atg18, indicating that Atg18 is not needed for this interaction (Fig. 1 C). Altogether, our results thus show that Atg9 binds Atg2, which in turn interacts with Atg18 (Fig. 1 D).

The interaction between Atg2 and Atg9 is essential for autophagy

To map the interaction site in Atg2, Y2H plasmids coding for C-terminal truncations of Atg2 were generated and analyzed with plasmids encoding AD-Atg9 on test plates. Atg9 was still able to bind the $Atg2^{1–1,268}$ truncation but not the $Atg2^{1–1,234}$ (Fig. 1 E). This result indicated that a stretch of 34 amino acids in Atg2 between positions 1,234 and 1,268 is responsible for the interaction with Atg9. Based on the Atg2 structural organization proposed by Kaminska et al. (2016), this region maps in the APT1 domain (Fig. 1 F). To identify the crucial binding site, we generated four point mutants where different sequences of polar and charged amino acids were mutated into alanines (Fig. 1 G) and analyzed these by Y2H against Atg9. Whereas $Atg2^{PM3}$ showed interaction with Atg9, $Atg2^{PM1}$, $Atg2^{PM2}$, and $Atg2^{PM4}$ did not (Fig. 1 H). These data provide evidence that this region is involved in Atg2 binding to Atg9.

We then expressed the generated point mutations in the *atg2Δ* strain to study the relevance of Atg2 binding to Atg9 in autophagy, and we performed autophagy flux assays in this background.

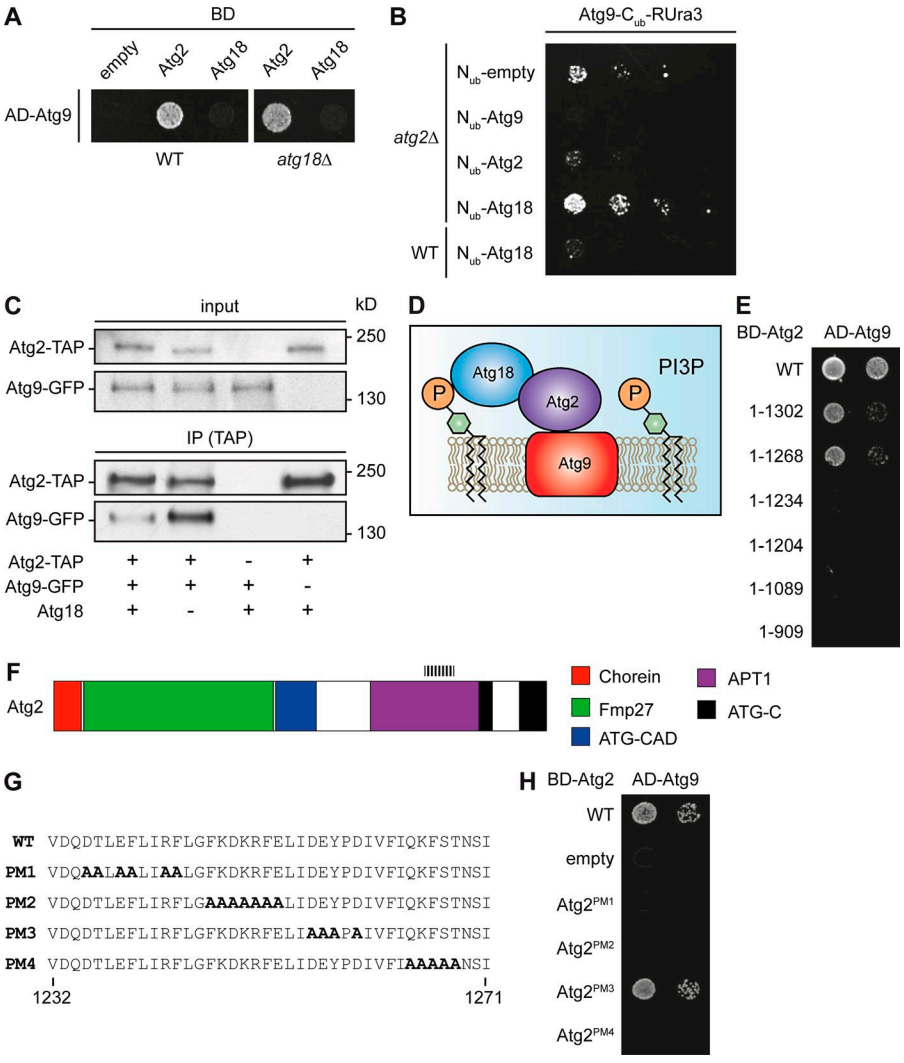

Figure 1. **Atg2 and Atg9 directly interact. (A)** Atg2–Atg9 interaction in different Y2H strains. Plasmids carrying the *ATG2* or *ATG9* gene fused with the BD or AD domains of the transcription factor Gal4, respectively, were transformed into Y2H WT (PJ69-4A) or *atg18Δ* (FRY382) strains. The pGBDU-C1 plasmid (empty) was used as a negative control. **(B)** Recapitulation of the Atg2–Atg9 interaction using the split-ubiquitin assay. All the split-ubiquitin constructs—pATG9_Cub_RURA3_Met313, pATG9_Nub_CUP_314, pATG18_Nub_CUP_314, and pATG2_Nub_Cub_314—were cotransformed into either WT (SEY6210) or *atg2Δ* (FRY383) cells. The pNub_CUP_314 plasmid was used as a negative control. **(C)** Atg18 is not required for the Atg2–Atg9 interaction. Cell extracts from *atg2Δ atg9Δ* (yDP29), *atg2Δ* Atg9-*GFP* (yDP191), and *atg2Δ atg18Δ* Atg9-*GFP* (yDP264) strains transformed with an empty vector (pRS315) or a plasmid expressing TAP-tagged Atg2 were subjected to pulldown experiments as described in Materials and methods. Immunoisolates were analyzed by Western blotting using anti-GFP and anti-TAP antibodies. **(D)** Model of the Atg9–Atg2–Atg18 complex. **(E)** A stretch of 34 amino acids between positions 1,232 and 1,268 of Atg2 is essential for the interaction with Atg9. Plasmids expressing the $Atg2^{1–1,302}$, $Atg2^{1–1,268}$, $Atg2^{1–1,204}$, $Atg2^{1–1,089}$, and $Atg2^{1–909}$ truncations were cotransformed with the vector carrying AD-Atg9 into the WT strain (PJ69-4A) before being assayed on the test plates. **(F)** Structural organization of Atg2 in domains as proposed (Kaminska et al., 2016). Through homology search (Finn et al., 2016), it appears that Atg2 possesses a Chorein-N domain (PF12624), a region with similarity to the mitochondrial protein FMP27 predicted to form a solenoid structure, an ATG2-CAD domain (PF13329) with unknown function, and a part similar to the Golgi APT1 protein of maize (PF10351). Additionally, the C terminus of Atg2 contains a region of high homology with the two mammalian Atg2 orthologues. It is composed of two ATG-C domains (PF09333) of unknown function. The first domain is truncated and lacks the distal part, whereas the second one is intact. The dashed lines indicate the identified region of Atg2 where the amino acids essential for its binding to Atg9 are localized. **(G)** Point mutants in Atg2. The Atg2 amino acid sequence between residues 1,232 and 1,271 is shown. The four Atg2 point mutants (PM1, PM2, PM3, and PM4) generated by replacing the charged and polar amino acids with alanines are indicated. The introduced alanines are in bold. **(H)** Interaction of point mutants with Atg9. BD-tagged Atg2 point mutants $Atg2^{PM1}$, $Atg2^{PM2}$, $Atg2^{PM3}$, and $Atg2^{PM4}$ were tested for their ability to bind AD-Atg9 in the WT strain (PJ69-4A) by Y2H assay. Only $Atg2^{PM3}$ was able to interact with Atg9.

The GFP-Atg8 processing assay is a well-established method to monitor the progression of bulk autophagy (Guimaraes et al., 2015). Upon autophagy induction, the GFP-Atg8 chimera is delivered by autophagosomes into the vacuole and processed to the protease-resistant GFP moiety, which can be traced over time. Free GFP accumulation in nitrogen-starved WT cells indicates normal progression of autophagy (Fig. 2 A). In contrast, no cleavage of GFP-Atg8 was observed in the *atg2Δ* mutant (Barth and Thumm, 2001; Shintani et al., 2001; Wang et al., 2001). Although the Atg9-interacting $Atg2^{PM3}$ as well as $Atg2^{PM2}$ constructs were able to complement the autophagy defect of the *atg2Δ* knockout as WT Atg2, $Atg2^{PM1}$ and $Atg2^{PM4}$ mutants failed to complement the *atg2Δ* cells.

We then validated these results using a different method, the Pho8Δ60 assay (Guimaraes et al., 2015). Upon induction of autophagy, the cytosolic Pho8Δ60 construct is delivered by autophagosomes into the vacuole lumen, where it is processed into an active form by resident proteases, which can be measured by a colorimetric assay. Pho8Δ60 activity was detected upon induction of autophagy in WT but not in *atg2Δ* cells (Fig. 2 B). $Atg2^{PM1}$ and $Atg2^{PM4}$ mutants had a similar defect, whereas $Atg2^{PM2}$ and $Atg2^{PM3}$ showed partial autophagic flux. A similar defect was observed for the processing of Ape1, a cargo of the constitutive cytosol-to-vacuole targeting pathway (Fig. 2 C; Lynch-Day and Klionsky, 2010). Although $Atg2^{PM2}$ did not seem to interact with Atg9 by Y2H, it appeared at least in part functional in vivo. In contrast, $Atg2^{PM1}$ and $Atg2^{PM4}$ perturb both Atg9 binding and nonselective and selective types of autophagy and therefore were analyzed further.

To determine whether the mutated amino acids in $Atg2^{PM1}$ and $Atg2^{PM4}$ are crucial to mediate the Atg2–Atg9 interaction in vivo, we purified Atg9-GFP from cells expressing TAP-tagged

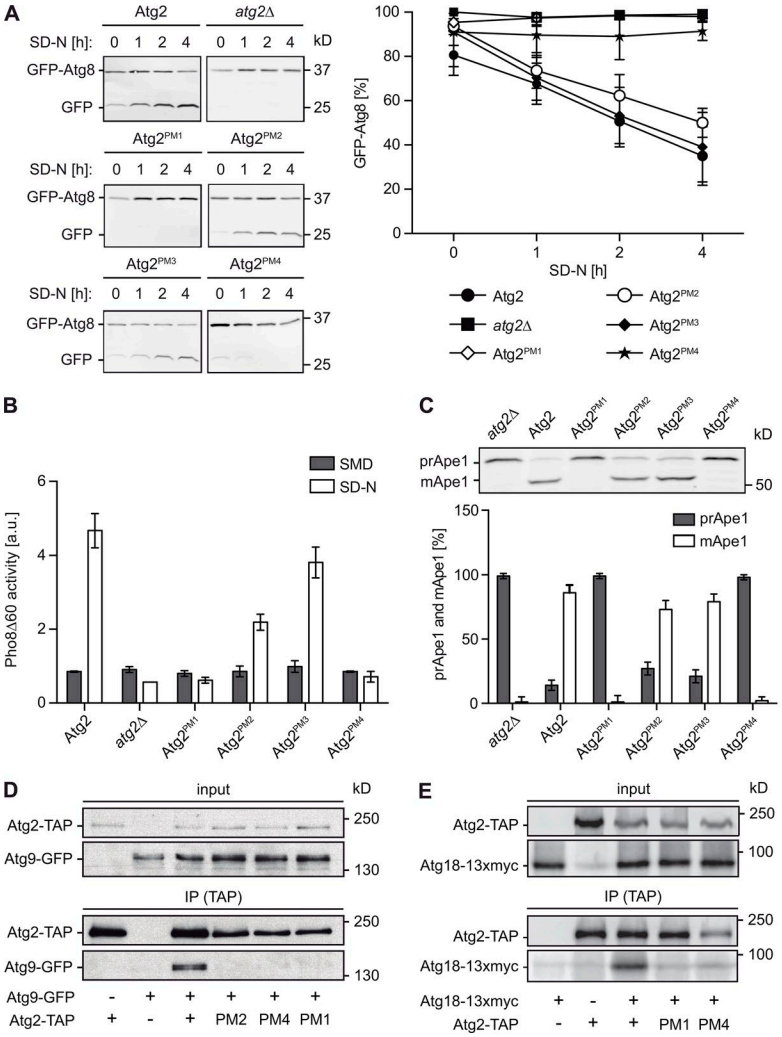

Figure 2. **Interaction between Atg2 and Atg9 is essential for both bulk and selective autophagy. (A)** Mutations in the putative Atg9-binding region of Atg2 lead to a severe block of bulk autophagy. The *atg2Δ* cells (FRY375) carrying both the pCuGFPATG8414 vector and a plasmid expressing Atg2 or the different Atg2 point mutants or the empty vector pRS416 were grown in SMD to an early log phase and transferred to the autophagy-inducing SD-N. Culture aliquots were collected 0, 1, 2, and 4 h after autophagy stimulation, and cell extracts were analyzed by Western blotting using an antibody against GFP. A graph representing the relative amount of the GFP-Atg8 chimera at each time point calculated from three independent experiments plus SD is shown on the right. Representative blots are shown on the left. **(B)** Defective autophagy caused by Atg2 mutations. The *PHO8Δ60 atg2Δ* strain (FRY388) was transformed with an empty vector (pRS416; *atg2Δ*) or plasmids expressing Atg2 or the different Atg2 point mutants. Transformed cells were cultured in SMD to early log phase and transferred into SD-N starvation medium for 4 h to induce autophagy. The Pho8Δ60 assay was performed as described in Materials and methods. **(C)** Mutations in the Atg9-binding region of Atg2 severely affect the cytosol-to-vacuole targeting pathway. Strains analyzed in A were cultured in SMD to early log phase. Samples were collected, and cell extracts were analyzed by Western blotting using the anti-Ape1 antiserum. The detected bands were then quantified as in A, and the percentages of precursor and mature Ape1 (prApe1 and mApe1, respectively) were plotted. The presented data represent the means of three independent experiments ± SD. **(D)** The identified Atg2^{PM1}, Atg2^{PM2}, and Atg2^{PM4} mutants do not interact with Atg9 in vivo. Cell extracts from *atg2Δ* (yCK759) and *atg2Δ* Atg9-*GFP* (yDP191) strains transformed with an empty vector (pRS315) or plasmids expressing WT or point-mutated TAP-tagged Atg2, pATG2^{PM1}-TAP, pATG2^{PM2}-TAP, and pATG2^{PM4}-TAP were subjected to pulldown experiments and analyzed as in Fig. 1 C. **(E)** Atg18 interaction with Atg2 requires Atg2 binding to Atg9. Cell extracts from *atg2Δ* (FRY375) and *atg2Δ* Atg18-13×myc strains transformed with an integrative empty vector (RSGY015) or plasmids expressing TAP-tagged versions of Atg2, Atg2^{PM1}, or Atg2^{PM4} (RSGY012, RSGY013, and RSGY014) were subjected to pulldown experiments and analyzed with anti-myc and anti-TAP antibodies.

Atg2, Atg2^{PM1}, or Atg2^{PM4}. Atg2^{PM1} and Atg2^{PM4} showed similar expression levels to WT Atg2 (Fig. 2 D, inputs). Although Atg2-TAP specifically pulled down Atg9-GFP, Atg9-GFP interacted with neither Atg2^{PM1}-TAP nor Atg2^{PM4}-TAP (Fig. 2 D, immunoprecipitation [IP]). We also analyzed Atg2^{PM2} in this pulldown analysis and observed no binding to Atg9-GFP. This shows that the mutations in Atg2^{PM2} weaken the interaction between this variant and Atg9 as suggested by the experiments measuring autophagy progression. To assess whether Atg2 binding to Atg9 also affected its interaction with Atg18, we repeated the assay with strains coexpressing Atg18-13×myc. As expected (Rieter et al., 2012), Atg2-TAP was able to specifically pull down Atg18 (Fig. 2 E). However, no interaction between Atg18-13×myc and both Atg2^{PM1}-TAP and Atg2^{PM4}-TAP was detected (Fig. 2 E). In line with this observation, Atg2–Atg18 association was severely affected in absence of Atg9 (Fig. S1, A and B).

Collectively, our data show that two amino acid patches within Atg2 between residues 1,235–1,243 and 1,264–1,268 are crucial for its binding to Atg9. Moreover, they also indicate that the Atg2 interaction with Atg9 plays an important role for association with Atg18.

Atg2 binding to Atg9 promotes its interaction with Atg18 on membranes

Atg18 possesses a PtdIns3P-binding motif that is required for its function in autophagy (Krick et al., 2006). In contrast, the Atg2 binding mechanism to lipid bilayers remains elusive and may depend on binding to Atg9. We therefore examined these interactions directly with liposomes and purified components. For this, we isolated full-length Atg9 and the Atg2–Atg18 complex via affinity purification from yeast (Fig. 3 A). In addition to the WT Atg2–Atg18 complex, we generated complexes with Atg2^{PM1} or Atg18^{FAAG}, a mutant unable to bind PtdIns3P (Dove et al., 2004; Krick et al., 2006), or both as controls. All complexes could be purified with similar efficiency (Fig. 3 A). Atg9 was then reconstituted into liposomes with or without PtdIns3P. As a control, liposomes lacking Atg9 were generated. We subsequently preincubated the different types of liposomes with the purified

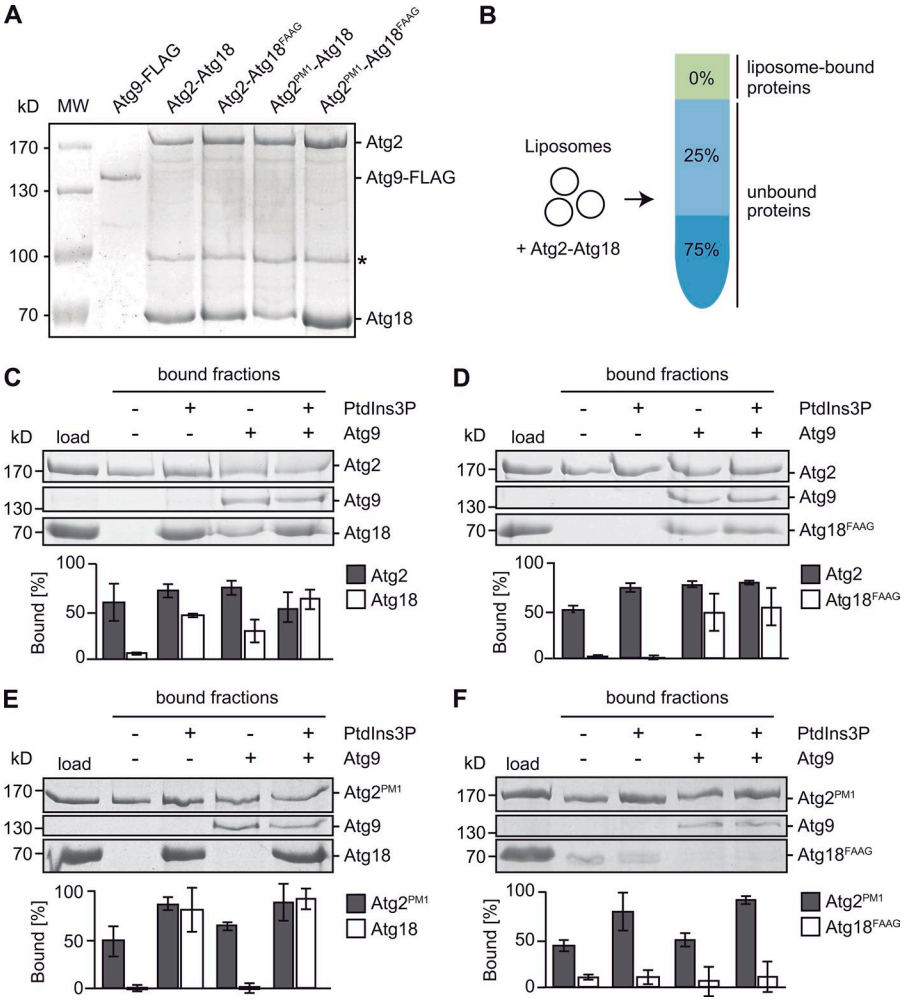

Figure 3. **Atg2 binding to Atg9 promotes its direct interaction with Atg18. (A)** Purified Atg9 and Atg2–18 complexes. Atg9-3×FLAG and Atg2–Atg18–TAP complexes were overproduced in yeast and purified as described in Materials and methods. Isolated proteins were separated by SDS-PAGE and visualized in gels with Coomassie staining. The asterisk indicates a degradation product. MW, molecular weight. **(B)** Schematic representation of liposome flotation assays. Liposomes containing or not containing Atg9 were incubated with purified Atg2–Atg18 complexes and mixed with 75% sucrose. Subsequent density centrifugation allowed separating unbound protein (bottom) from liposomes with bound protein (top). **(C–F)** Interaction of Atg2 and Atg18 with liposomes. Liposomes consisting of 69–72 mol% DOPC, 15 mol% DOPE, 12 mol% DOPS, 0.5 mol% Atto550-DPPE, and 0 or 3 mol% PtdIns3P were reconstituted with or without purified Atg9 in a 1:1,000 protein/lipid ratio. Top fractions of different liposome species incubated with purified Atg2–Atg18 (C), Atg2–Atg18^{FAAG} (D), Atg2^{PM1}–Atg18^{FAAG} (E), or Atg2^{PM1}–Atg18 (F) were TCA precipitated and loaded on SDS-PAGE gel. To analyze the amount of bound protein, gels were stained with Coomassie, and band intensities were quantified using ImageJ. The graphs show mean quantifications of three independent experiments ± SD.

Atg2–Atg18 complexes and then separated liposomes with bound protein (top) from unbound protein (bottom) via a sucrose gradient (Fig. 3 B). With the WT Atg2–Atg18 complex, we detected Atg2 on liposomes independently of the presence of PtdIns3P or Atg9 (Fig. 3 C, lane 2). In contrast, Atg18 association was dependent on PtdIns3P (lanes 2 and 3), indicating that Atg2 alone does not recruit Atg18 to membranes. Based on our quantification, we estimate a stoichiometry of ∼1:1:1 ratio between Atg9–Atg2–Atg18. If liposomes lacked PtdIns3P but contained Atg9, ≤50% of Atg18 was found on membranes with Atg2 (lane 4), indicating that Atg2 binding to Atg9 indeed increases its affinity for Atg18 (Fig. 3 C).

As controls, we performed the same binding assay with different complex combinations, i.e., Atg2–Atg18^{FAAG} and Atg2^{PM1}–Atg18 and Atg2^{PM1}–Atg18^{FAAG}. As expected, Atg18^{FAAG} was not recruited by PtdIns3P, but ≤58% of the protein was still detected on Atg9-containing liposomes (Fig. 3 D). Intriguingly, the recruitment of Atg18 in absence of PtdIns3P was completely abolished when Atg18 or Atg18^{FAAG} were incubated with Atg2^{PM1} (Fig. 3, D and E). In those situations, the quantified ratio between Atg9–Atg2–Atg18 was ∼1:1:0. This result, together with our findings above, indicates that the interaction of Atg2 with Atg9 directly drives the interaction of Atg18 with Atg2, possibly via an Atg9-induced conformational change in Atg2. Of note, although PtdIns3P or Atg2–Atg9 were sufficient to recruit Atg18 onto membranes in vitro, it is known that yeast strains expressing Atg18^{FAAG} or Atg18^{L2}, an Atg2-binding mutant of Atg18, are just able to sustain minimal autophagic activity (Rieter et al., 2012). Therefore, it is likely that the recruitment of Atg18 onto membranes in vivo depends on both PtdIns3P and the Atg2–Atg9 interaction. Surprisingly, Atg2 was binding to liposomes with a similar efficiency independently of the presence of Atg9 (Fig. 3, C–F), whereas the recruitment seemed slightly increased when liposomes contained PtdIns3P (Fig. 3, D–F). Altogether, these analyses show that Atg2 directly binds to lipid bilayers in vitro and that its interaction with Atg9 promotes Atg18 recruitment to membranes.

Atg2 recognizes membranes via PtdIns3P and lipid-packing defects

We next examined which properties are required for Atg2 association onto membranes using giant unilamellar vesicles (GUVs). We incubated overexpressed Atg2-mGFP purified from yeast together with fluorescent GUVs with the same lipid composition as the liposomes and then imaged the distribution of this fusion protein. Surprisingly, we found that Atg2 localizes in distinct patches scattered on the GUV membranes (Fig. 4 A). In contrast with the control GUVs, where the fluorescent lipid Atto550-1,2-Bis(diphenylphosphino)ethane (DPPE) was homogenously distributed along the membrane, the lipid was enriched

in the Atg2-mGFP–positive patches. In particular, Atg2 and Atto550-DPPE colocalized in randomly distributed patches of sizes from 300 nm to 2 µm that cover ≤15% of the membrane area. Because fluorescent probes such as rhodamine-DPPE, which is closely related to Atto550-DPPE, prefer to partition in liquid disordered (L_D) domains (Juhasz et al., 2012), we hypothesized that lipid packing may play a role in Atg2 interaction with membranes. Cone-shaped lipids are known to induce lipid-packing defects, i.e., L_D, and phosphatidylethanolamine (PE) is one of them. To test for the possible preference of Atg2 for binding to L_D domains, we omitted PE from our lipid mixture used to generate GUVs, leaving just PtdIns3P and the two cylindrical-shaped lipids phosphatidylcholine and phosphatidylserine. Under these conditions, neither Atg2 association nor partitioning of Atto550-DPPE into distinct patches was observed (Fig. 4, B and C). Ergosterol with its small head group and sterol backbone can also induce lipid-packing defects like PE. Importantly, we observed Atg2 binding and Atto550-DPPE clustering in membranes of GUVs, where we replaced PE for ergosterol. This result further supports the notion that Atg2 associates with membranes carrying lipid-packing defects.

It has been reported that Atg2 has a domain that is able to bind phosphoinositides, with a preference for PtdIns3P (Kaminska et al., 2016). In our liposome flotation assays, we only detected minor differences in the amounts of Atg2 bound to liposomes with or without PtdIns3P (Fig. 3, C–F). We thus asked whether PtdIns3P is involved in Atg2 recruitment onto lipid bilayers. We observed no Atg2-GFP association with GUVs when PtdIns3P was omitted irrespective of lipid-packing defects caused by PE (Fig. 4, B and C). The recruitment and distribution on GUVs was similar when Atg2 was purified from *atg18Δ* cells (Fig. 5 A). Importantly, $Atg2^{PM1}$ associated to GUVs similarly to WT Atg2, indicating that the introduced mutations do not alter the lipid-binding properties of this protein (Fig. 5 B).

We thus conclude that Atg2 recognizes PtdIns3P and lipid packing defects. We assume that Atg2 binding to membranes is less dependent on PtdIns3P in the liposome assays as the membranes are severely curved and therefore contain more lipid-packing defects.

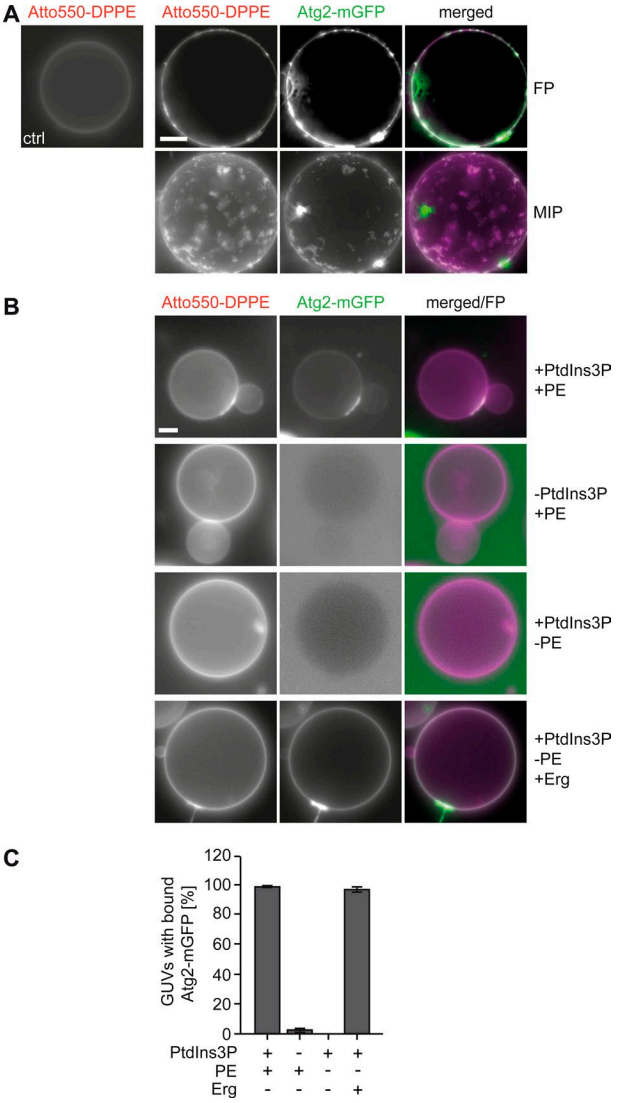

Figure 4. **Atg2 requires PtdIns3P and lipid-packing defects to tightly associate with membranes in vitro. (A)** GUVs with the same lipid composition as the liposomes used in Fig. 3 were incubated with either 400 nM purified Atg2-mGFP or an equal volume of buffer (control) for 5 min at room temperature before being imaged. Single focal plane (FP) images and maximum-intensity projections (MIPs) of 62 optical planes are shown. **(B)** Analysis of Atg2-mGFP binding to GUVs with different compositions. Where indicated, the lipid mixture used in A was altered by substituting 15 mol% DOPE(PE) with equal molarities of DOPC or ergosterol (erg), whereas 3 mol% PtdIns3P was replaced by an equal molarity of DOPC. Bars, 10 µm. **(C)** Quantification of Atg2-mGFP binding to GUVs of the experiment shown in B. At least 30 GUVs per sample were counted, and the graph represents means of three independent experiments ± SD.

Atg2 binding to Atg9 is essential for its correct localization at the PAS

Because the Atg2 recruitment to lipid bilayers was Atg9 independent, we next analyzed whether GFP-tagged $Atg2^{PM1}$ and $Atg2^{PM4}$ could still localize to the PAS by fluorescence microscopy. As expected, Atg2 was mostly found in a single punctuate structure per cell in both growing and starvation conditions (Fig. 6, A and B), which represents the PAS (Shintani et al., 2001; Wang et al., 2001; Suzuki et al., 2007). In contrast, $Atg2^{PM1}$-GFP and $Atg2^{PM4}$-GFP failed to distinctively associate to the PAS but also any other organelle, suggesting a possible recruitment defect to this site.

Atg2 is essential for Atg18 recruitment to the PAS (Obara et al., 2008; Rieter et al., 2012), and therefore we explored whether its interaction with Atg9 is required for the correct localization of Atg18. Atg18 is also present on endosomes and the vacuole surface (Guan et al., 2001; Dove et al., 2004; Krick et al., 2008; Obara et al., 2008). To specifically analyze its pool on autophagosomal membranes, we used mCherry-tagged Atg8 as the specific marker protein (Suzuki et al., 2007; Mari et al., 2010). As shown in Fig. 6 (C and D), presence of Atg2 allowed the correct association of part of Atg18 to the PAS, whereas *ATG2* deletion blocked this event in both nutrient-rich and -poor conditions. Complementation of the *atg2Δ* knockout with either $Atg2^{PM1}$ or $Atg2^{PM4}$ could not bypass the Atg18 recruitment defect of these cells, reinforcing the notion that Atg2 presence at the PAS is essential for Atg18

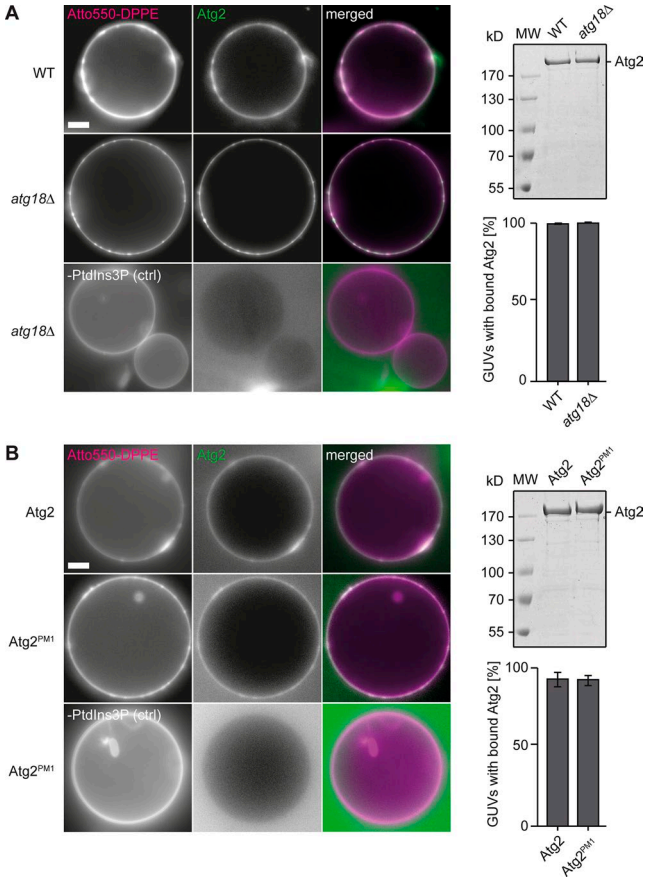

Figure 5. **Atg2 and Atg2^{PM1} bind membranes similarly. (A)** Atg2-mGFP isolated from WT or *atg18Δ* cells was incubated with GUVs as in Fig. 4 A. GUVs without PtdIns3P were used as controls. Binding to GUVs was quantified as described in Materials and methods. **(B)** Purified and DY-647–labeled Atg2 or Atg2^{PM1} were incubated with GUVs, and binding was quantified and controlled as in A. At least 30 GUVs per sample were counted, and graphs represent means of three independent experiments ± SD. Bars, 10 µm. MW, molecular weight.

localization to this site. Unexpectedly, however, Atg18 could be observed at the PAS in the strain expressing Atg2^{PM4} when cells were deprived of nutrients, indicating that Atg2^{PM4} retains some weak ability to recognize Atg18 (see Discussion).

In the absence of Atg2, Atg9 accumulates at the PAS, and this had led to the hypothesis that Atg2 is required for Atg9 retrieval from autophagosomal membranes (Reggiori et al., 2004). To determine whether normal Atg9 distribution requires direct interaction with Atg2, we scrutinized Atg9-GFP localization in cells expressing Atg2^{PM1} and Atg2^{PM4} by fluorescence microscopy in both growing and starvation conditions. Atg9-GFP localized in several punctuate structures in cells carrying endogenous or ectopically expressed Atg2 as previously reported (Fig. 7, A and B; Reggiori et al., 2004; Mari et al., 2010; Ohashi and Munro, 2010; Yamamoto et al., 2012). In agreement with previous literature (Reggiori et al., 2004), deletion of *ATG2* caused a concentration of Atg9-GFP to a predominant perivacuolar punctum. Importantly, the same phenotype was observed in the *atg2Δ* strain carrying Atg2^{PM1} or Atg2^{PM4}, indicating that Atg9 requires binding to Atg2 for its correct subcellular distribution.

In WT cells, Atg2 mainly localizes to the extremities of the phagophore together with Atg9 and Atg18 (Graef et al., 2013; Suzuki et al., 2013). Therefore, we asked whether the inability of Atg9 to interact with Atg2 was altering its distribution on the phagophore surface by taking advantage of an approach where overexpression of Ape1 leads to the formation of a giant Ape1 oligomer, and then a larger phagophore accumulates around it (Suzuki et al., 2013). As shown previously (Graef et al., 2013; Suzuki et al., 2013), Atg9-GFP was mostly confined to the edges of phagophores (visualized with mCherry-Atg8) and adjacent to the giant BFP-Ape1 in cells carrying Atg2 (Fig. 7, C and D). Deletion of *ATG2* resulted in a single punctuate structure positive for both mCherry-Atg8 and Atg9-GFP, underlying again the fact that Atg2 could be involved in the formation of phagophores. In contrast, these membranous cisternae were present in cells expressing Atg2^{PM1} and Atg2^{PM4}. More importantly, Atg9 localized to the edges as in the WT strain, showing that Atg2 does not determine the positioning of Atg9 on the phagophore.

Collectively, these results show that Atg9 trafficking to the PAS and its localization to the extremities of the growing phagophore do not require its binding to Atg2. The interaction between Atg2 and Atg9, however, is required for the correct association of Atg2 to PAS and subsequent recruitment of Atg18.

Atg2^{PM1} and Atg2^{PM4} are recruited to the PAS but have altered distribution on the phagophore

Atg2 concentrates at the extremities of the phagophore together with Atg9 and Atg18 (Graef et al., 2013; Suzuki et al., 2013). The observations that Atg18 can be recruited to the PAS in Atg2^{PM4}-expressing cells and that Atg2 can associate with membranes irrespective of the presence of Atg9 both in vivo and in vitro (Figs. 3, 4, 5, and 6) led us to hypothesize that Atg2^{PM1} and Atg2^{PM4} might be recruited to autophagosomal membranes but have a different distribution. Atg2 is poorly expressed (Ghaemmaghami et al., 2003), and the failure of concentrating in discrete assemblies could make it undetectable by fluorescence microscopy. Therefore, we turned to the bimolecular fluorescence complementation (BiFC) approach (Sung and Huh, 2007). This assay allows studying close proximity between different proteins in vivo. It is based on the formation of a fluorescent complex by the C- and N-terminal fragments of Venus, a variant of the YFP, which are fused to two proteins of interest. Venus has also a better signal-to-noise ratio than GFP and allows the detection of weak fluorescent signals. We created strains expressing solely or in combination Atg2 and Atg1 endogenously tagged with the N-terminal fragment of Venus (VN) and the C-terminal fragment of Venus (VC), respectively. We opted for Atg1 as this protein is distributed on the entire phagophore surface (Graef et al., 2013; Suzuki et al., 2013). In cells expressing only one of the fusion proteins, i.e., Atg1-VC, no fluorescence signal was detected (Fig. 8, A and B). In the strains carrying both, Atg1-VC and Atg2-VN, or Atg2^{PM1}-VN or Atg2^{PM4}-VN, in contrast, a clear BiFC signal concentrating to a single perivacuolar punctuate structure was detected (Fig. 8, A and B). Colocalization of the reconstituted Venus signals with mCherryV5-Atg8 revealed that Atg2^{PM1} and Atg2^{PM4} were recruited to the PAS, where they were probably not concentrated in a peculiar microdomain of the phagophore and thus remained

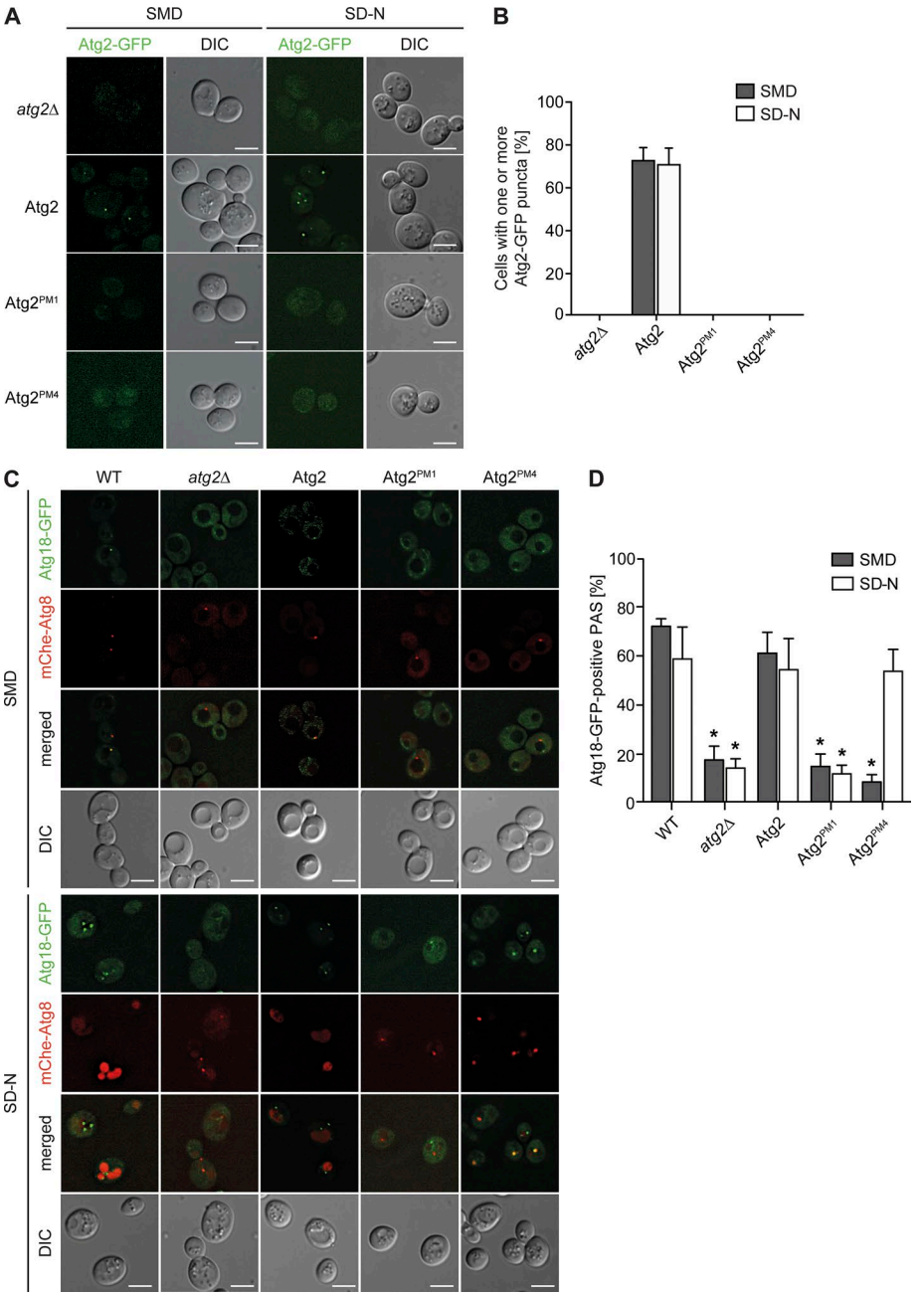

Figure 6. **Atg2^{PM1} and Atg2^{PM4} mutants are not normally distributed to the PAS. (A)** Cellular distribution of Atg2-GFP variants in *atg2Δ*cells (FRY375) transformed with plasmids expressing Atg2-GFP, Atg2^{PM1}-GFP, or Atg2^{PM4}-GFP. Strains were grown to an early log phase before being nitrogen starved for 3 h. Cells were imaged by fluorescence microscopy before and after nitrogen starvation. **(B)** Quantification of the percentage of cells with one or more Atg2-GFP–positive dot in the experiment presented in A. **(C)** Atg2 binding to Atg9 is required for Atg18 recruitment to the PAS. Cellular distribution of endogenous Atg18-GFP in WT (RSGY017) or *atg2Δ* (RSGY018) carrying mCherryV5-Atg8 fusion protein and transformed with integrative plasmids expressing TAP-tagged versions of Atg2 (pATG2-TAP(405); RSGY019), Atg2^{PM1} (pATG2^{PM1}-TAP(405); RSGY020), or Atg2^{PM4} (pATG2^{PM4}-TAP(405); RSGY021) strains. Strains were grown to an early log phase before being nitrogen starved for 3 h. Cells were imaged by fluorescence microscopy before and after nitrogen starvation. DIC, differential interference contrast. Bars, 5 µm. **(D)** Quantification of the percentage of cells with colocalizing puncta presented in C. Graphs represent means of three experiments ± SD. Asterisks highlight significant differences with the strain carrying WT Atg2.

(eventually) undetectable when fused to GFP. These BiFC signals were specific because Atg1-VC and Atg2-VN showed no interaction with cytoplasmic VN and VC, respectively (Fig. S1, C and D).

While performing this experiment, we had the impression that cells expressing Atg2^{PM1} and Atg2^{PM4} had a PAS/phagophore that was bigger than the one in the *atg2Δ* mutant. Although the number of observed PAS/phagophores was identical in Atg2^{PM1}- and Atg2^{PM4}-expressing cells and to the one in the *atg2Δ* knockout, the fluorescence signal intensity and size of the mCherry-Atg8–positive puncta was higher (Fig. 8, C and D). This indicates that these mutant proteins did not affect the formation rate of this specialized site, although they may affect its morphology. To more carefully analyze the PAS/phagophore, we also opted for a yeast background, i.e., W303, which generates larger autophagosomes than other commonly used strain backgrounds (Graef et al., 2013). As shown in Fig. S2 (A and B), cells lacking *ATG2* and strains carrying Atg2^{PM1} and Atg2^{PM4} had the same amount of PAS/phagophores. The fluorescence signal intensity and size of the mCherry-Atg8–positive puncta, in contrast, were higher in the cells carrying Atg2^{PM1} and Atg2^{PM4} than in the *atg2Δ* knockout. This result supports the notion that the presence of these two Atg2 variants allows the formation of the phagophore but probably not its expansion into an autophagosome (Fig. S2, A and C). To corroborate these fluorescence microscopy observations, we also assessed the levels of lipidated Atg8, i.e., Atg8-PE, by Western blotting. Indeed, Atg8-PE amounts were significantly higher in the strains carrying Atg2^{PM1} or Atg2^{PM4} compared with the *atg2Δ* mutant (Fig. S2, D and E).

Finally, to confirm that Atg2^{PM1} and Atg2^{PM4} have a different distribution on the phagophore than WT Atg2, we repeated the

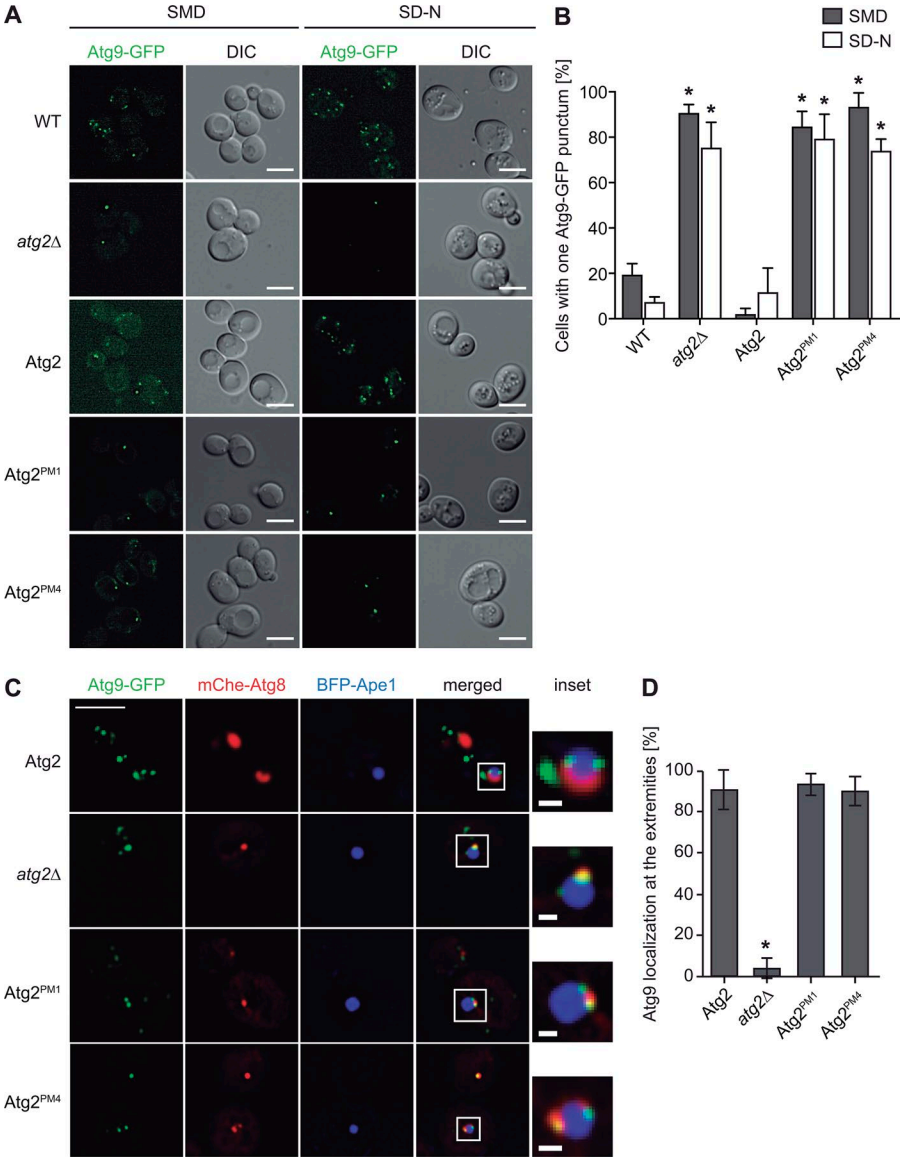

Figure 7. **Atg9 interaction with Atg2 is required for Atg9 normal subcellular distribution. (A)** Localization of endogenous Atg9-GFP in WT (KTY97) or *atg2Δ* (SAY118) cells transformed with integrative plasmids expressing TAP-tagged versions of Atg2 (pATG2-TAP(405); RSGY003), Atg2^{PM1} (pATG2^{PM1}-TAP(405); RSGY004), or Atg2^{PM4} (pATG2^{PM4}-TAP(405); RSGY005) strains was analyzed. DIC, differential interference contrast. **(B)** Quantification of the percentage of cells displaying a single Atg9-GFP punctum in the experiment shown in A. **(C)** Examination of Atg9-GFP distribution on the phagophores adjacent to giant Ape1 by fluorescence microscopy. The *atg2Δ* mutant expressing Atg9-GFP and mCherry-Atg8 (CUY10934) was transformed with the pDP105 plasmid and analyzed as described in Materials and methods. Bars: (main images) 5 µm; (insets) 1 µm. **(D)** Statistical evaluation of phagophores displaying Atg9-GFP at their extremities. Graphs represent means of three experiments ± SD. Asterisks highlight significant differences with the strain carrying WT Atg2.

BiFC analysis but with Atg9 instead of Atg1 as Atg9 concentrates at the extremities of the phagophore in Atg2^{PM1}- and Atg2^{PM4}-expressing cells (Fig. 7, C and D). Although we could detect a BiFC signal between Atg9-VC and Atg2-VN at the PAS, no interaction was observed between Atg9-VC and Atg2^{PM1}-VN or Atg2^{PM4}-VN (Fig. 8, E and F). This result agrees with the fact that Atg2^{PM1} and Atg2^{PM4} are unable to interact with Atg9, but it also highlights that these mutant proteins do not efficiently localize to the phagophore extremities.

To more precisely determine the distribution of Atg2^{PM1} and Atg2^{PM4} on the phagophore surface, we opted again for the giant Ape1 strategy. Strains expressing mCherryV5-Atg8, Atg1-VC and Atg2-VN, or Atg2^{PM1}-VN or Atg2^{PM4}-VN were transformed with a plasmid, allowing the overexpression of giant BFP-Ape1. As shown in Fig. 9 A, the BiFC signal was mostly localized at the edges of the phagophore in cells carrying WT Atg2-VN as expected (Graef et al., 2013; Suzuki et al., 2013). Remarkably, this fluorescence signal was distributed on the phagophore surface in cells expressing Atg2^{PM1}-VN or Atg2^{PM4}-VN (Fig. 9, A and B), indicating that Atg2 binding to Atg9 restricts this protein to the extremities of the phagophore. As Atg18-GFP is recruited to the PAS in nitrogen-starved cells expressing Atg2^{PM4} (Fig. 6, C and D), we also analyzed its distribution on the phagophore in a strain producing giant Ape1. Atg18-GFP was recruited less efficiently to phagophores in these cells in comparison with the strain carrying WT Atg2 (Fig. S2, F and G). When detected, Atg18-GFP was at the extremities of the phagophore, revealing that this protein in principle localizes similarly as Atg9. It is likely that a subpopulation of Atg2^{PM4} is also at this location rather than redistributed over the entire surface of the phagophore like Atg2^{PM1}. This observation further supports the notion that Atg18 binding to Atg2 requires the interaction of this latter protein with Atg9. Collectively, our data show that Atg2^{PM1} and Atg2^{PM4} are both recruited to the PAS and that although they allow the formation of the phagophore, their defect in binding Atg9 leads to their aberrant distribution on this precursor structure.

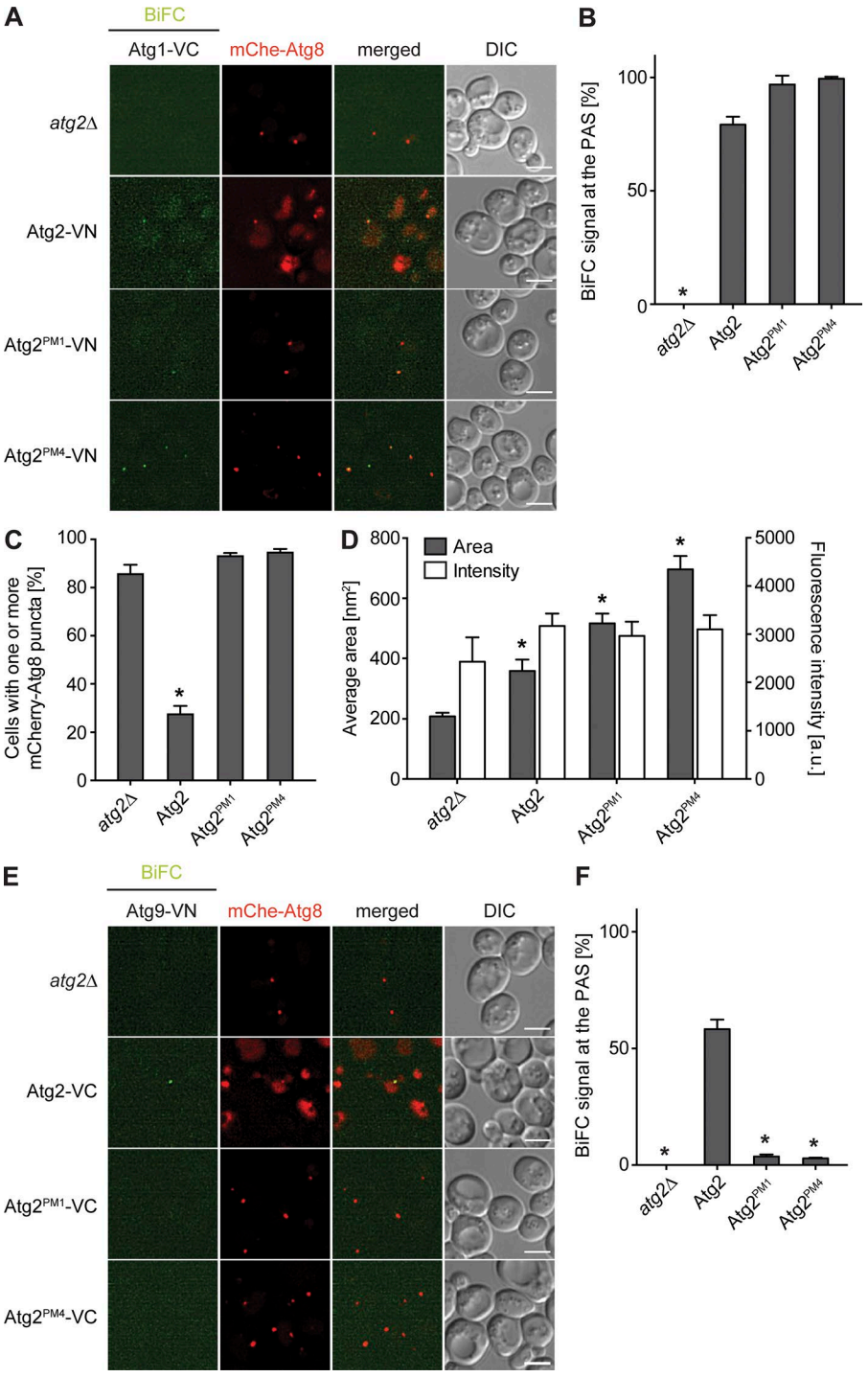

Figure 8. **Atg2^{PM1} and Atg2^{PM4} are recruited to the PAS, but they have altered distribution on the phagophore. (A)** Atg2 localization at the PAS was visualized by BiFC. Strains (RSGY087, RSGY089, and RSGY090) expressing both endogenous Atg1-VC and Atg2-VN, Atg2^{PM1}-VN, or Atg2^{PM4}-VN and carrying a mCherryV5-Atg8 construct were grown to an early log phase in YPD before being nitrogen starved for 3 h and imaged. Cells (RSGY088) expressing only Atg1-VC and mCherryV5-Atg8 were used as controls. **(B)** Quantification of the percentage of BiFC puncta colocalizing with mCherry-Atg8 in the experiment shown in A. **(C)** Quantification of percentage of cells that present at least one mCherryV5-Atg8 punctum in A. **(D)** Quantification of the mean size in nm^2 and intensity of the fluorescent signal in a.u. of mCherryV5-Atg8 puncta depicted in A. Data analysis was performed as described in Materials and methods. **(E)** Atg2–Atg9 interaction at the PAS was visualized by BiFC. Strains (RHY031, RHY032, and RHY033) expressing both endogenous Atg9-VN and Atg2-VC, Atg2^{PM1}-VC, or Atg2^{PM4}-VC and carrying a pCumCherryV5ATG8 construct were processed as in A. Cells (RHY030) expressing only Atg9-VN and mCherryV5-Atg8 were used as a control. DIC, differential interference contrast. Bars, 5 µm. **(F)** Quantification of the percentage of BiFC puncta colocalizing with mCherry-Atg8 in the experiment shown in E. Graphs represent means of three independent experiments ± SD. Asterisks highlight significant differences with the strains expressing WT Atg2 (B and F) or *atg2Δ* (C and D) cells.

Atg2 establishes contact between autophagosomal membranes and the ER

To examine whether the inability of Atg2 to both bind Atg9 and correctly localize would affect the organization of the PAS, we took advantage of an immunoelectron tomography (IET) method that we have developed for yeast (Mari et al., 2014) to resolve the PAS area at the ultrastructural level in cells expressing Atg2^{PM1} and Atg2^{PM4}. The PAS was immunolocalized using antibodies against Ape1 (Mari et al., 2010) as the oligomer formed by this protease localizes to the PAS in absence of Atg2 or in cells carrying Atg2^{PM1} and Atg2^{PM4} (Fig. S3, A and B). In the *atg2Δ* mutant, we observed the presence of the ER in the reconstructed region of the PAS from time to time (Video 1), which in certain cases was adjacent to the Ape1 oligomer (Video 2). Astonishingly, the ER was in close proximity to the Ape1 oligomer, sometimes around almost its entire surface, in several of the reconstructions obtained from cells expressing Atg2^{PM1} or Atg2^{PM4} (Videos 3 and 4). To substantiate these observations, we quantified ER proximity to the Ape1 oligomer in all the collected tomograms, which provide reconstructions of 150–200 nm cross-sections through the PAS area. We defined three categories. The first was *no ER* and included those situations where the ER was not observed or was observed at a distance

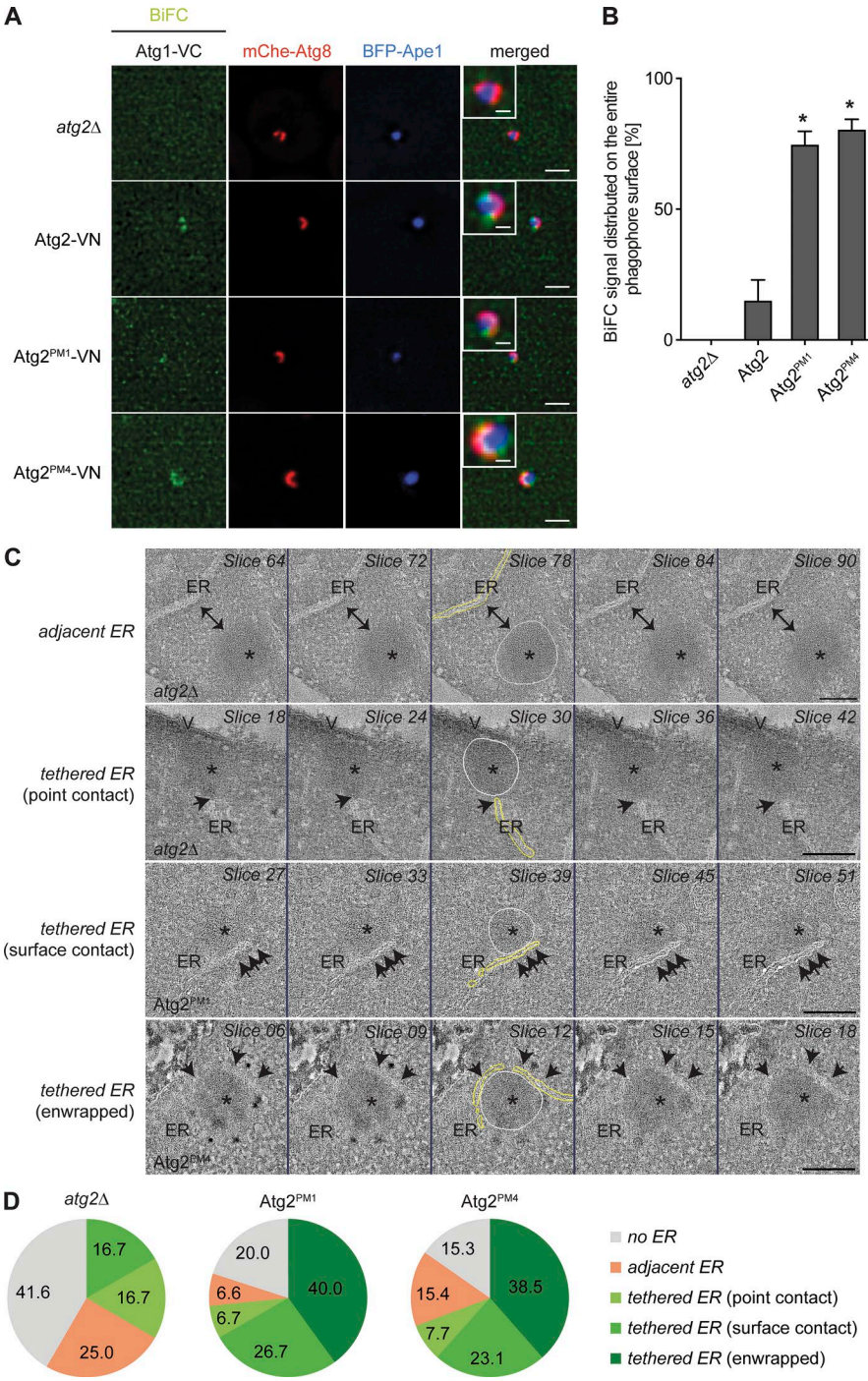

Figure 9. **The PAS and the ER are in close association in Atg2^{PM1}- and Atg2^{PM4}-expressing cells. (A)** Strains analyzed in Fig. 8 A (RSGY087, RSGY088, RSGY089, and RSGY090) were transformed with the pDP245 plasmid and grown to an exponential phase before adding 250 µM of $CuSO_4$ 4 h before reaching 0.6 OD_{600}. At that point, 400 nM of rapamycin was added, and incubation was continued for an additional 3 h. Bars: (main images) 1 µm; (insets) 300 nm. **(B)** Quantification of the percentage of BiFC signal detected on the entire surface of the mCherry-Atg8–positive phagophore and not on its extremities in the experiment shown in A. The graph represents the mean of three experiments ± SD. Asterisks indicate significant differences with the strain carrying WT Atg2. **(C)** Cryosections of 250–300 nm from either the *atg2Δ* mutant or cells expressing Atg2^{PM1} or Atg2^{PM4} were labeled with an anti-Ape1 antibody (10 nm gold; indicated with red spheres in videos). Using a conventional electron microscope, the areas of interest were selected based on the immunogold labeling, and dual-tilt series were recorded using a 200-kV transmission electron microscope. Tomographic slices (inverted grayscale) extracted from different tomograms illustrating different types of association between the Ape1 oligomer and the ER. Single- and double-direction arrows indicate the region of contact and the distance, respectively, between the Ape1 oligomer and the ER. The contours of the Ape1 oligomer (white) and of the ER (yellow) are shown in the middle panels. V, vacuole. Asterisks indicate Ape1 oligomers. Bars: (adjacent ER) 156 nm; (tethered ER) 184 nm. Representative examples of types of associations are also shown as 3D reconstructions in Videos 1 (Ape1 oligomer in the *atg2Δ* mutant with adjacent ER at a distance between 30 and 150 nm), 2 (Ape1 oligomer in the *atg2Δ* strain with an ER tethered with a single *point of contact*), 3 (Ape1 oligomer in Atg2^{PM1}-expressing cells with an ER tethered with a *surface contact*), and 4 (Ape1 oligomer in Atg2^{PM1}-expressing cells with an ER tethered with *enwrapping*). **(D)** Quantification of the different Ape1–ER contacts profiles described in the text in the three analyzed strains in C.

>150 nm from the Ape1 oligomer. The second category was *adjacent ER* and described those cases where the ER was at a distance between 30 and 150 nm from the Ape1 oligomer (Fig. 9 C, top row). The third, *tethered ER*, grouped all those situations where the ER was proximal to the Ape1 oligomer at <30 nm. This latter category was further subdivided in *point contact* (Fig. 9 C, second row), *surface contact* (Fig. 9 C, third row), and *enwrapped* (Fig. 9 C, bottom row) groups, which defined the lengths of the ER contact site with the Ape1 oligomers, i.e., <40 nm, 40–160 nm, and >160 nm, respectively. This classification of the results confirmed that the presence of the Atg2^{PM1} or Atg2^{PM4} variants enhances the close association between the ER and the Ape1 oligomer (Fig. 9 D). Examination and morphometrical quantification of the ER by electron microscopy showed that these changes were not caused by a major ultrastructural alteration of this organelle or its expansion. The mean ER surface per cell section in strains expressing Atg2, Atg2^{PM1}, and Atg2^{PM4} was 0.9, 1.2, and 1.0 µm^2, respectively, and the observed differences were not significant. Our IET method made it difficult to optimally preserve the phagophore because its membranes are mostly composed of lipids and therefore difficult to be immobilized. Although we could not detect the phagophore at the interface between the ER and the oligomer, we could observe this cisterna bordering the Ape1 oligomer in some reconstructions of strains carrying Atg2^{PM1} or Atg2^{PM4} (Fig. S3, C and D; and Videos 5 and

6). Similarly to what has been reported for mammalian cells (Axe et al., 2008; Hayashi-Nishino et al., 2009; Ylä-Anttila et al., 2009; Uemura et al., 2014), the detected phagophores appeared as very thin dark membranes and close to the ER, yet not continuous.

In yeast, fluorescence microscopy analyses have shown that the PAS is adjacent to both the vacuole and the ER (Graef et al., 2013; Suzuki et al., 2013). Because of the IET observations, we next explored whether the disruption of the Atg2–Atg9 interaction could affect this subcellular positioning. We thus determined the distribution of the PAS, identified using the mCherryV5-Atg8 chimera, relative to the ER and vacuole in strains lacking *ATG2* or carrying Atg2^{PM1} and Atg2^{PM4}. The ER was visualized by fusing Sec63, an ER-resident protein, with GFP, and the vacuole was labeled with the specific dye 7-amino-4-chloromethylcoumarin (CMAC). As expected (Graef et al., 2013; Suzuki et al., 2013), the PAS was very often (i.e., >80%) localized in proximity of both the ER and the vacuole in growing and starved cells expressing WT Atg2 (Fig. S4). Deletion of *ATG2* or presence of Atg2^{PM1} and Atg2^{PM4}, however, did not alter this distribution. We concluded that Atg2 is not required for the overall subcellular positioning of the PAS.

To more specifically study the phagophore and its close association to the ER, we took advantage of the giant Ape1 approach again. We thus overproduced BFP-Ape1 in the *atg2Δ* knockout and in Atg2^{PM1}- and Atg2^{PM4}-expressing cells. All these strains also carried the marker proteins mCherry-Atg8 and Sec63-GFP to visualize the phagophore and the ER, respectively. In agreement with the IET data, we found that most of the phagophores (>70%) in the cells carrying Atg2^{PM1} and Atg2^{PM4} were closely associated with the ER (Fig. 10, A and B). This profile was not observed in the *atg2Δ* mutant, where we only detected points of contacts between the ER and PAS as for the ER and phagophore of WT cells (Fig. 10, A and B; Graef et al., 2013; Suzuki et al., 2013). These strains were also analyzed by IET, which confirmed the close association between PAS and ER in cells expressing Atg2^{PM1} and Atg2^{PM4} (Videos 7 and 8). The ER tethering had a surface contactor enwrapped profile in 55.6% (Atg2^{PM1}) and 66.7% (Atg2^{PM4}) of the reconstructions. In the WT strain (Video 9), these two profiles were not detected, and the ER was only observed with a point contactor in the vicinity of the PAS in 81.8% of all reconstructions. Finally, we also explored the relevance of Atg9 in the formation of phagophores in WT and Atg2^{PM1}- or Atg2^{PM4}-expressing cells in the presence of giant Ape1. In all strains, deletion of *ATG9* resulted in a single punctuate PAS, which was mostly adjacent to the ER (Fig. S5). This result was expected as Atg9 plays a key role in the phagophore biogenesis (Mari et al., 2010; Rao et al., 2016; Yamamoto et al., 2016).

Collectively, our data show that the presence of Atg2 at the PAS promotes both formation of the phagophore and its contact with the ER. Failure of interacting with Atg9, however, causes an aberrant Atg2-dependent connection with the ER and probably blocks phagophore expansion.

Discussion

Although it is a core component of the Atg machinery, the function of Atg2 in autophagosome biogenesis remains unknown. Atg2 has been physically and genetically connected to Atg9 and Atg18, but how these three Atg proteins associate was unclear (Barth and Thumm, 2001; Shintani et al., 2001; Wang et al., 2001; Reggiori et al., 2004; Suzuki et al., 2007; Obara et al., 2008; Rieter et al., 2012). Our in vivo data reveal that Atg2 interacts with Atg9, and in agreement with the previous observation that Atg2 can be recruited to the PAS in the absence of Atg18 (Rieter et al., 2012), this binding is required for the subsequent association of Atg18 to Atg2. Our in vitro results support this notion as Atg2 binding to Atg9 enhances recruitment of Atg18 onto liposomes. Therefore, the simplest model is that Atg2 association to Atg9 induces a conformational change that, together with the presence of PtsIns3P on autophagosomal membranes, promotes the specific recruitment of Atg18. It has been previously suggested that Atg2 and Atg18 form a constitutive complex that is recruited to the PAS as a single unit (Obara et al., 2008). Although our observations appear to be in apparent contradiction with this result, we isolated Atg2–Atg18 as a complex from yeast for our in vitro experiments. This suggests that once formed, the Atg2–Atg18 complex could form a stable structure that would need to be disengaged possibly once an autophagosome is completed and/or released in the cytoplasm.

To understand the relevance of the Atg9–Atg2 interaction in autophagy, we have identified the region in Atg2 localized between amino acids 1,232 and 1,271 that is important for its binding to Atg9. Alignment of this part of Atg2 with that of homologues present in other species (Fig. 10 C) shows that the region containing the amino acids mutated in Atg2^{PM1} is highly conserved, indicating that the mechanism of interaction between Atg2 and Atg9 could be shared within eukaryotes. The amino acids mutated in Atg2^{PM4}, in contrast, are less conserved, and they appear to be distant from those of Atg2^{PM1} in the mammalian proteins (Fig. 10 C). A speculative idea would be that the residues mutated in Atg2^{PM4} are either part of a regulatory sequence or that their change into alanines indirectly affects the conformation of the putative Atg9-binding site. These considerations could also explain why cells expressing Atg2^{PM1} and Atg2^{PM4} do not display completely identical phenotypes, i.e., phagophore are easily detectable and Atg18 can be recruited to the PAS under starvation conditions in Atg2^{PM4}-expressing cells but not in the ones carrying Atg2^{PM1}.

Although it remains to be dissected at the molecular level how the identified amino acids modulate Atg2–Atg9 interaction, the Atg2^{PM1} and Atg2^{PM4} mutants have been pivotal in helping to understand the functional relationship between Atg2 and Atg9. The first important observation is that we could detect phagophores using different experimental approaches in cells expressing Atg2^{PM1} and Atg2^{PM4}, which have not been observed in this study and before in the *atg2Δ* knockout. These data suggest that Atg2 could have additional functions in the autophagosome biogenesis outside the context of the Atg9–Atg2–Atg18 functional cluster, possibly by playing a role in either the formation of the phagophore and/or its initial expansion phases. A second key result obtained with the Atg2^{PM1} and Atg2^{PM4} variants is that Atg9 is not essential for Atg2 recruitment onto autophagosomal membranes. Our in vitro data, which are consistent with recent studies on lipid binding of yeast Atg2 and mammalian ATG2B

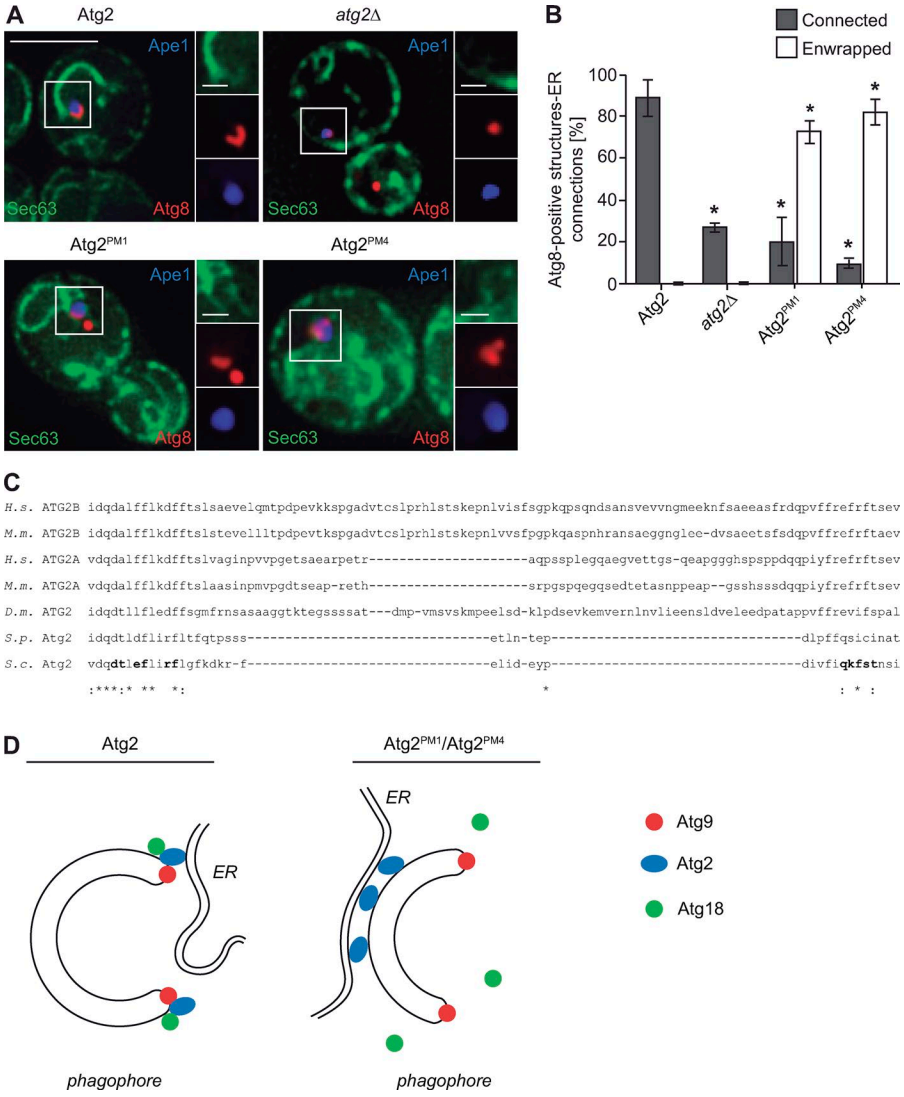

Figure 10. **Atg2 determines the contact sites between the phagophore and the ER. (A)** Analysis of the ER–phagophore connection in cells generating giant Ape1 by fluorescence microscopy. The *atg2Δ* mutant expressing Sec63-GFP and mCherry-Atg8 (CUY10935) was transformed with both pDP105 and the pRS416 empty vector or a plasmid expressing Atg2 (pYCG_YNL242w), Atg2^{PM1} (pYCG_YNL242w_PM1), or Atg2^{PM4} (pYCG_YNL242w_PM4). The resulting strains were grown in SMD to an early log phase before to induce the formation of giant Ape1 as described in Materials and methods and to image the cells. Bars: (main images) 5 µm; (insets) 1 µm. **(B)** Quantification of the type of ER association to the mCherry-Atg8–positive phagophore in the experiment shown in C. Enwrapped defines all those situations when the ER was tethered to almost the entire surface of the phagophore, and Connected is when there was at least one point of contact between the ER and the phagophore. The graph represents the mean of three experiments ± SD. Asterisks indicate significant differences with cells expressing WT Atg2. **(C)** Conservation among species of the Atg2 residues involved in Atg9 binding. The amino acid sequence of *S. cerevisiae* (*S.c.*) Atg2 between residues 1,232 and 1,271 was aligned with that of *Homo sapiens* (*H.s.*) ATG2A and ATG2B, *Mus musculus* (*M.m.*) ATG2A and ATG2B, *Drosophila melanogaster* (*D.m.*), and *Schizosaccharomyces pombe* (*S.p.*) Atg2 using the Clustal Omega program (http://www.ebi.ac.uk/Tools/msa/clustalo/). The amino acids mutated in Atg2^{PM1} and Atg2^{PM4} are in bold. Asterisks indicate conservation of the residue, and colons designate similarity. **(D)** Left: Atg9 is confined at the extremities of the phagophore, where Atg2 also gets specifically concentrated by binding to this transmembrane protein. Atg9–Atg2 association also promotes the Atg18 recruitment, and collectively, these three factors play a key role in generating phagophore–ER contact sites at this location, although those appear to be preferentially generated at one of the two edges of the phagophore. Right: Inability of Atg2^{PM1} and Atg2^{PM4} to bind Atg9 impairs their targeting at the ends of the growing phagophore and Atg18 recruitment to this precursor structure. Redistribution of Atg2^{PM1} and Atg2^{PM4} on the phagophore surface leads to the formation of more extensive, wrongly positioned, and likely nonfunctional contact sites with the ER.

(Kaminska et al., 2016; Zheng et al., 2017), show that Atg2 can associate to membranes by direct binding to lipids including PtdIns3P. Because the tested lipids are present on other subcellular organelles, this implies that there should be another binding determinant on autophagosomal membranes, possibly another component of the Atg machinery. Nonetheless, our data demonstrate that Atg2 binding to Atg9 is required for confining Atg2 to the extremities of the growing phagophore, where Atg9 concentrates independently from its interaction with Atg2 (and Atg18). Atg2 failure in interacting with Atg9 leads to Atg2 distribution over all the surface of the phagophore and a concomitant defect in autophagy.

Which function does Atg2 have at the extremities of the growing phagophore? A crucial clue emerged from our IET analyses, which revealed that Atg2 influences the association of the ER with the PAS. It has previously been documented that the ER is very often positioned in close proximity to the phagophore extremities (Graef et al., 2013; Suzuki et al., 2013). Based on this observation and others, our hypothesis is that Atg9 allows positioning Atg2 to this specific region of the phagophore, which in turn mediates the establishment of contact sites with the ER (Fig. 10 D, left). In agreement with previous studies (Graef et al., 2013; Suzuki et al., 2013), we also observed one of the two edges of the phagophore in association with the ER by fluorescence microscopy

and IET analyses. Atg2 variants unable to bind Atg9 fail to get confined at the extremities of the phagophore and disperse on its surface, where they can still tether the ER (Fig. 10 D, right). These expanded phagophore–ER contact sites are probably not functional because factors such as Atg18 are not recruited, and as a result, autophagosome biogenesis is severely impaired. However, we cannot exclude that the autophagy block observed in cells expressing Atg2^{PM1} and Atg2^{PM4} is caused by a defect in Atg9 cycling (Fig. 7, A and B) or by other functions of either Atg2 or Atg18. Very interestingly, Atg2 shares amino acid sequence similarities with Vps13, a protein that in yeast has been shown to participate in vacuole–mitochondria, endosome–mitochondria, and nucleus–vacuole contact sites (Lang et al., 2015; Park et al., 2016; John Peter et al., 2017). As one of the putative functions of membrane contact sites is lipid transfer from a donor to an acceptor organelle (Jain and Holthuis, 2017), a speculative idea is that the Atg9–Atg2–Atg18 complex is required to establish a line of lipid transport from the ER into the phagophore to supply at least in part the enormous demand in membranes required for autophagosome biogenesis. Alternatively, this contact may balance the specific lipid composition of autophagosomes. Other scenarios, however, are also possible. In conclusion, our results reveal a key role of Atg2 in connecting the membranes of nascent autophagosomes with the ER. Future studies are required to determine which is the precise molecular function of this protein and its interactors, i.e., Atg9 and Atg18, in this specialized subdomain of the phagophore.

Materials and methods

Strains and media

The *Saccharomyces cerevisiae* strains used in this study are listed in Table 1. For gene disruptions, coding regions were replaced with genes expressing auxotrophic markers or antibiotic resistance genes using PCR primers containing ∼60 bases of identity to the regions flanking the ORF (Longtine et al., 1998; Janke et al., 2004). Gene knockouts were verified by examining Ape1 processing by Western blotting using a polyclonal antibody against Ape1 (Mari et al., 2010) and/or PCR analysis of the deleted gene locus.

Chromosomal tagging of the *ATG1*, *ATG2*, *ATG9*, *ATG18*, and *SEC63* genes at the 3′ end with *GFP*, *13×myc*, *VN*, and *VC* was performed using PCR-based integration of the sequence encoding for the tag using pFA6a-GFP(S65T)-TRP1 and pFA6a-GFP(S65T)-HIS5, pFA6a-13myc-TRP1, pFA6a-VC-TRP1, and pFA6a-VN-His3MX6 plasmids as templates (Longtine et al., 1998; Sung and Huh, 2007). Chromosomal tagging was verified by Western blot analysis using antibodies against the myc epitope (Invitrogen) or GFP (Roche).

Yeast cells were grown in rich (YPD [1% yeast extract, 2% peptone, and 2% glucose] or YPG [1% yeast extract, 2% peptone, and 2% galactose]) or synthetic minimal media (SMD; 0.67% yeast nitrogen base, 2% glucose, and amino acids and vitamins as needed). Starvation experiments were conducted in synthetic media lacking nitrogen (SD-N; 0.17% yeast nitrogen base without amino acids and 2% glucose) or by treating the cells with 200 ng/ml rapamycin (LC Laboratories).

Plasmids

For the construction of the Y2H plasmids, a DNA fragment encoding *ATG2* was generated by PCR using *S. cerevisiae* genomic DNA as a template and cloned as an XmaI–SalI fragment into the pGBDU-C1 vector (James et al., 1996). The C-terminal truncations of *ATG2* (i.e., pGBDU-Atg2$^{1–1,302}$, pGBDU-Atg2$^{1–1,268}$, pGBDU-Atg2$^{1–1,204}$, pGBDU-Atg2$^{1–1,089}$, pGBDU-Atg2$^{1–909}$, pGBDU-Atg2$^{1–668}$, pGBDU-Atg2$^{1–333}$, pGBDU-Atg2$^{1–194}$, and pGBDU-Atg2$^{1–92}$) were generated by PCR using a 5′ primer that introduces an XmaI restriction site just before the start codon of the gene and a 3′ primer specific for each truncation, which introduces a stop codon followed by a SalI restriction site. These truncations were also cloned as XmaI–SalI fragments into the pGBDU-C1 plasmid. The point mutations in *ATG2* were introduced by PCR using appropriate primers exploiting the unique PmlI restriction site in the sequence of *ATG2*, which is in close proximity with the stretch of nucleotides of interest. For each point mutant, a specific 5′ primer was used that contained the PmlI restriction site and introduced the point mutations and a 3′ primer that introduced a SalI restriction site after the stop codon of the full-length *ATG2*. The PCR fragments were then cloned into the pGBDU-Atg2 plasmid using PmlI and SalI, creating pGBDU-Atg2^{PM1} (D1235A, T1236A, E1238A, F1239A, R1242A, and F1243A), pGBDU-Atg2^{PM2} (F1246A, K1247A, D1248A, K1249A, R1250A, F1251A, and E1252A), pGBDU-Atg2^{PM3} (D1255A, E1256A, Y1257A, and D1259A), and pGBDU-Atg2^{PM4} (Q1264A, K1265A, F1266A, S1267A, and T1268A). The pGAD-Atg9 plasmid was a gift from D.J. Klionsky (He et al., 2008).

Fragments containing the *ATG2* point mutants were subcloned into the pYCG_YNL242w plasmid (Euroscarf), which carried the *ATG2* gene including its own promoter and terminator (Barth and Thumm, 2001), using BlpI and BsiWI. This generated the pYCG_YNL242w_PM1, pYCG_YNL242w_PM2, pYCG_YNL242w_PM3, and pYCG_YNL242w_PM4 plasmids.

The pCK364/pATG2-TAP315 plasmid, which expresses Atg2-TAP under the control of the endogenous *ATG2* promoter, has been described previously (Papinski et al., 2014). The mutations of *ATG2* were swapped from the pYCG_YNL242w_PM1, pYCG_YNL242w_PM2, and pYCG_YNL242w_PM4 plasmids into pCK364 using the unique BsiWI and MscI restriction sites in *ATG2*. This led to the creation of pATG2^{PM1}-TAP315, pATG-2^{PM2}-TAP315, and pATG2^{PM4}-TAP315 plasmids. Transfer into pRS405 generated integration versions of the same vectors: pATG2-TAP405, pATG2^{PM1}-TAP405, pATG2^{PM2}-TAP405, and pATG2^{PM4}-TAP405.

Plasmids pATG2-VN405, pATG2-VC405, pATG2^{PM1}-VN405, pATG2^{PM1}-VC405, pATG2^{PM4}-VN405, and pATG2^{PM4}-VC405 were created by PCR amplifying *VN* and *VC* from the pFA6a-VN-His3MX6 and pFA6a-VC-TRP1 vectors, respectively, and replacing the sequence coding for the TAP tag in the pATG2-TAP405, pATG2^{PM1}-TAP405, and pATG2^{PM4}-TAP405 plasmids using PacI–XhoI. Control plasmids expressing VN and VC under the control of the *ATG2* and *ATG1* promoter, respectively, were generated by replacing the *ATG2* gene in the pATG2-VN405 and pATG2-VC405 vectors ∼560 bp upstream with *ATG2* and *ATG1* start codons using NotI and PacI. This procedure lead to the creation of the promATG2-VN405 and promATG1-VC405 constructs.

Table 1. **Strains used in this study**

Name	Genotype	Origin
BY4741	*MATa his3Δ1 leu2Δ0 met15Δ0 ura3Δ0*	Brachmann et al. (1998)
BY4742	*MATα his3Δ1 leu2Δ0 lys2Δ0 ura3Δ0*	Brachmann et al. (1998)
BY4747	*MATα his3Δ200 leu2Δ0 lys2Δ0 met15Δ0 trp1Δ63 ura3Δ0*	Brachmann et al. (1998)
CUY4813	BY4741 *hphNT1::GAL1pr-ATG2-*m*GFP-TAP::kanMX*	This study
CUY9058	BY4741xB4727 *URA3::GAL1pr-ATG18-TAP::kanMX hphNT1::GAL1pr-ATG2*	This study
CUY10110	BY4727 *NatMX6::prGAL1-ATG9-3xFLAG::hphNT1*	This study
CUY10771	BY4741 *hphNT1::GAL1pr-ATG2 GAL1pr-ATG18^{FAAG}-TAP::URA3*	This study
CUY10811	BY4727 *atg2Δ::hphNT1 URA3::GAL1pr-ATG18-TAP::kanMX cloNAT::GAL1pr-ATG2^{PM1}::TRP1*	This study
CUY10813	BY4727 *atg2Δ::hphNT1 GAL1pr-ATG18^{FAAG}-TAP::URA3 cloNAT::GAL1pr-ATG2^{PM1}::TRP1*	This study
CUY10934	SEY6210 *ATG9-GFP::hphNT1 natNT2::ADH1pr-mCherry-ATG8 atg2Δ::HIS5S.p.*	This study
CUY10935	SEY6210 *SEC63-GFP::kanMX natNT2::ADH1pr-mCherry-ATG8 atg2Δ::HIS5S.p.*	This study
CUY11160	BY4741 *hphNT1::GAL1pr-ATG2-*m*GFP-TAP::kanMX atg18Δ::NatNT2*	This study
CUY11161	BY4727 *CloNAT::GAL1pr-ATG2^{PM1}-TAP::kanMX-TRP1 atg2Δ::hphNT1*	This study
ERY087	SEY6210 *ATG2-GFP::HIS5S.p. atg18Δ::TRP1*	Rieter et al. (2012)
FRY375	SEY6210 *atg2Δ::HIS5S.p.*	This study
FRY382	PJ69-4A *atg18Δ::TRP1*	This study
FRY383	SEY6210 *atg2Δ::LEU2*	This study
FRY388	BY4742 *pho13Δ::kanMX pho8::PHO8Δ60 atg2Δ::HIS5S.p.*	This study
KTY97	SEY6210 *ATG9-GFP::TRP1*	Reggiori et al. (2004)
PJ69-4A	*MATa leu2-3,112 trp1-Δ901 ura3-52 his3-Δ200 galΔ4 gal80Δ LYS::GAL1-HIS3 GAL2-ADE2 met2::GAL7-lacZ*	James et al. (1996)
RGY296	SEY6210 *atg8Δ::kanMX atg2Δ::hphNT1 SEC63-GFP::NatMX6 pCumCheV5ATG8::URA3 pRS::TRP1*	This study
RGY303	SEY6210 *atg8Δ::kanMX atg2Δ::hphNT1SEC63-GFP::NatMX6 pCumCheV5ATG8::URA3 pATG2::TRP1*	This study
RGY304	SEY6210 *atg8Δ::kanMX atg2Δ::hphNT1 SEC63-GFP::NatMX6 pCumCheV5ATG8::URA3 pATG2^{PM1}::TRP1*	This study
RGY305	SEY6210 *atg8Δ::kanMX atg2Δ::hphNT1 SEC63-GFP::NatMX6 pCumCheV5ATG8::URA3 pATG2^{PM4}::TRP1*	This study
RGY528	SEY6210 *atg8Δ::LoxP-kanMX-LoxP pCumCheV5ATG8::URA3 ATG18-GFP::NatMX6 atg2Δ::hphNT1 pRS405::LEU2*	This study
RGY529	SEY6210 *atg8Δ::LoxP-kanMX-LoxP pCumCheV5ATG8::URA3 ATG18-GFP::NatMX6 atg2Δ::hphNT1 pATG2-TAP::LEU2*	This study
RGY530	SEY6210 *atg8Δ::LoxP-kanMX-LoxP pCumCheV5ATG8::URA3 ATG18-GFP::NatMX6 atg2Δ::hphNT1 pATG2^{PM1}-TAP::LEU2*	This study
RGY531	SEY6210 *atg8Δ::LoxP-kanMX-LoxP pCumCheV5ATG8::URA3 ATG18-GFP::NatMX6 atg2Δ::hphNT1 pATG2^{PM4}-TAP::LEU2*	This study
RGY562	SEY6210 *ATG18 × 13myc::TRP1 atg2Δ::HIS5S.p. pATG2-TAP::LEU2 atg9Δ::URA3K.l.*	This study
RHY030	SEY6210 *ATG9-VN::HIS3 atg2Δ::TRP1 pCumCheV5ATG8::URA3*	This study
RHY031	SEY6210 *ATG9-VN::HIS3 atg2Δ::TRP1 pCumCheV5ATG8::URA3 pATG2-VC::LEU2*	This study
RHY032	SEY6210 *ATG9-VN::HIS3 atg2Δ::TRP1 pCumCheV5ATG8::URA3 pATG2^{PM1}-VC::LEU2*	This study
RHY033	SEY6210 *ATG9-VN::HIS3 atg2Δ::TRP1 pCumCheV5ATG8::URA3 pATG2^{PM4}-VC::LEU2*	This study
RHY034	SEY6210 *SEC63-GFP::kanMX natNT1:: ADH1pr-mCherry-ATG8 atg2Δ::HIS5S.p. atg9Δ::TRP1*	This study
RHY038	SEY6210 *ATG1-VC::TRP1 atg2Δ::hphMX6 promATG2-VN::LEU2 pCumCheV5ATG8::URA3*	This study
RHY040	SEY6210 *ATG2-VN::HIS5S.p. pCumCheV5ATG8::URA3 promATG1-VC::LEU2*	This study
RSGY003	SEY6210 *ATG9-GFP::TRP1 atg2Δ::HIS5S.p. pATG2-TAP::LEU2*	This study
RSGY004	SEY6210 *ATG9-GFP::TRP1 atg2Δ::HIS5S.p. pATG2^{PM1}-TAP::LEU2*	This study
RSGY005	SEY6210 *ATG9-GFP::TRP1 atg2Δ::HIS5S.p. pATG2^{PM4}-TAP::LEU2*	This study

Table 1. **Strains used in this study *(Continued)***

Name	Genotype	Origin
RSGY011	SEY6210 *ATG18 × 13myc::TRP1 atg2Δ::HIS5S.p.*	This study
RSGY012	SEY6210 *ATG18 × 13myc::TRP1 atg2Δ::HIS5S.p. pATG2-TAP::LEU2*	This study
RSGY013	SEY6210 *ATG18 × 13myc::TRP1 atg2Δ::HIS5S.p. pATG2^{PM1}-TAP::LEU2*	This study
RSGY014	SEY6210 *ATG18 × 13myc::TRP1 atg2Δ::HIS5S.p. pATG2^{PM4}-TAP::LEU2*	This study
RSGY015	SEY6210 *ATG18 × 13myc::TRP1 atg2Δ::HIS5S.p. pRS::LEU2*	This study
RSGY017	SEY6210 *ATG18-GFP::TRP1 pCumCheV5ATG8::URA3*	This study
RSGY018	SEY6210 *ATG18-GFP::TRP1 pCumCheV5ATG8::URA3 atg2Δ::HIS5S.p.*	This study
RSGY019	SEY6210 *ATG18-GFP::TRP1 pCumCheV5ATG8::URA3 atg2Δ::HIS5S.p. pATG2-TAP::LEU2*	This study
RSGY020	SEY6210 *ATG18-GFP::TRP1 pCumCheV5ATG8::URA3 atg2Δ::HIS S.p. pATG2^{PM1}-TAP::LEU2*	This study
RSGY021	SEY6210 *ATG18-GFP::TRP1 pCumCheV5ATG8::URA3 .atg2Δ::HIS5S.p pATG2^{PM4}-TAP::LEU2*	This study
RSGY024	SEY6210 *atg2Δ::HIS5S.p. pRS::LEU2 pCumCheV5ATG8::URA3*	This study
RSGY025	SEY6210 *atg2Δ::HIS5S.p. pATG2^{PM1}-TAP::LEU2 pCumCheV5ATG8::URA3*	This study
RSGY026	SEY6210 *atg2Δ::HIS5S.p. pATG2^{PM4}-TAP::LEU2 pCumCheV5ATG8::URA3*	This study
RSGY040	W303 *pCumCheV5Atg8::URA3 atg2Δ::TRP1*	This study
RSGY041	W303 *pCumCheV5Atg8::URA3 atg2Δ::HIS5S.p. pATG2-TAP::LEU2*	This study
RSGY042	W303 *pCumCheV5Atg8::URA3 atg2Δ::HIS5S.p. pATG2^{PM1}-TAP::LEU2*	This study
RSGY043	W303 *pCumCheV5Atg8::URA3 atg2Δ::HIS5S.p. pATG2^{PM4}-TAP::LEU2*	This study
RSGY052	W303 *atg2Δ::TRP1 pATG2-TAP::LEU2*	This study
RSGY053	W303 *atg2Δ::TRP1*	This study
RSGY054	W303 *atg2Δ::TRP1 pATG2^{PM1}-TAP::LEU2*	This study
RSGY055	W303 *atg2Δ::TRP1 pATG2^{PM4}-TAP::LEU2*	This study
RSGY087	SEY6210 *ATG1-VC::TRP1 atg2Δ::hphMX6 pATG2-VN::LEU2pCumCheV5ATG8::URA3*	This study
RSGY088	SEY6210 *ATG1-VC::TRP1 atg2Δ::hphMX6 pCumCheV5ATG8::URA3*	This study
RSGY089	SEY6210 *ATG1-VC::TRP1 atg2Δ::hphMX6 pATG2^{PM1}-VN::LEU2pCumCheV5ATG8::URA3*	This study
RSGY090	SEY6210 *ATG1-VC::TRP1 atg2Δ::hphMX6 pATG2^{PM4}-VN::LEU2pCumCheV5ATG8::URA3*	This study
SAY118	SEY6210 *ATG9-GFP::TRP1 atg2Δ::HIS5S.p.*	This study
SEY6210	*MATα ura3-52 leu2-3,112 his3-Δ200 trp1-Δ901 lys2-801suc2-Δ9 mel GAL*	Robinson et al. (1988)
VDY101	SEY6210 *atg7Δ::LEU2*	Lab stock
W303	*MATα ade2–1 leu2–3 his3–11, 15 trp1–1 ura3–1 can1–100*	Graef et al. (2013)
yCK759	BY4742 *atg2Δ::kanMX*	This study
yDP29	BY4741 *atg2Δ:: hphNT1 atg9Δ::kanMX*	This study
yDP191	BY4741 *MET15 atg2Δ::kanMX ATG9-GFP::URA3*	This study
yDP264	BY4741 *MET15 atg2Δ::kanMX atg18Δ::kanMX*	This study

The vector expressing Atg2-GFP from the authentic promoter, i.e., pATG2GFP(416), was created by amplifying the *ATG2-GFP* sequence from the genome of the ERY087 strain and cloned as a SacII–XhoI fragment into pRS416. The mutations of *ATG2* were transferred from the pYCG_YNL242w_PM1 and pYCG_YNL242w_PM4 plasmids into pATG2GFP(416) using the unique BlpI and BamHI restriction sites in *ATG2*, generating the pATG2^{PM1}GFP(416) and pATG2^{PM4}GFP(416) vectors.

The plasmids for the split-ubiquitin assay were constructed as follows. DNA fragments encoding *ATG2*, *ATG9*, and *ATG18* were generated by PCR using *S. cerevisiae* genomic DNA as a template. *ATG9* was cloned as a ClaI–SalI fragment into the pCub_RURA3_Met313 vector to generate the pATG9_Cub_RURA3_Met313 plasmid (Wittke et al., 1999). *ATG9*, *ATG2*, and *ATG18* plus 300 bp of their terminator sequences were cloned as BclI–KpnI fragments into the pNub_CUP_314 plasmid.

The pRS315 (empty integrative vector), pRS404 (empty integrative vector), pRS405 (empty integrative vector), pRS416 (empty centromere [CEN] vector), pCuGFPATG8(414) (CEN plasmid expressing GFP-Atg8 under the control of the *CUP1* promoter), pCumCheV5ATG8(406) (integrative plasmid expressing mCherry-V5-Atg8 under the control of the *CUP1* promoter), pDP105/pRS315-CUP1pr-BFP-APE1 (CEN plasmid expressing BFP-Ape1 under the control of the *CUP1* promoter), pDP245/pRS313-CUP1pr-BFP-Ape1 (CEN plasmid expressing BFP-Ape1 under the control of the *CUP1* promoter), and pTS466 (CEN

plasmid expressing GFP-Ape1 under the control of the authentic promoter) plasmids have been described previously (Sikorski and Hieter, 1989; Kim et al., 2002; Shintani et al., 2002; Mari et al., 2010; Pfaffenwimmer et al., 2014).

Y2H and split-ubiquitin assays

The plasmids pGAD-C1 and pGBDU-C1 carrying *ATG9* and *ATG2* or their mutated and truncated forms were transformed into the different Y2H strains (Table 1) and grown on SMD lacking leucine and uracil (James et al., 1996). Colonies, which contain both vectors, were then spotted on SMD lacking histidine, leucine, and uracil. When both proteins interact, the reporter gene HIS3 is transcribed, and the test strain grows on plates lacking histidine.

The pATG9_Cub_RURA3_Met313 and pNub_CUP_314 plasmids harboring the *ATG2*, *ATG9*, or *ATG18* genes were transformed into WT (SEY6210) or *atg2Δ* (FRY383) cells and grown on SMD lacking tryptophan and histidine. Colonies carrying both plasmids were restricted on SMD plates lacking tryptophan, histidine, and uracil and supplemented with 250 µM methionine (Wittke et al., 1999). The modified *URA3* gene in the pCub_RURA3_Met313 vector was used as reporter for the interaction. Reconstitution of ubiquitin upon interaction between the two proteins of interest led to the degradation of Ura3 by ubiquitin-specific proteases. As a result, the transformed cells were not able to grow on the test plates.

Protein A affinity purifications

For the experiments shown in Figs. 1 C and 2 D, cells were grown in 100 ml YPD to 2 OD_{600} before treatment with 220 nM rapamycin (LC Laboratories) for 1 h. Then, 150 OD_{600} equivalents were collected by centrifugation at 3,000 *g* for 10 min, washed with PBS supplemented with 2% glucose, and collected again by centrifugation at 3,000 *g* for 5 min. Cells were resuspended in 300 µl Pho-IP buffer (20 mM Pipes, pH 6.8, 0.5% Triton X-100, 50 mM KCl, 100 mM potassium acetate, 10 mM $MgSO_4$, 10 µM $ZnSO_4$, and 500 µM DTT supplemented with 1 mM PMSF, 1 mM NaF, 1 mM Na_3VO_4, 20 mM β-glycerophosphate, and cOmplete protease inhibitor cocktail [Roche]) and lysed using glass beads and vortexing at 4°C. Cell lysates were cleared twice by centrifugation at 16,000 *g* for 10 min at 4°C. Lysate protein concentrations were determined by a Bradford assay and equalized by dilution in Pho-IP buffer. Aliquots of 15 µg protein were collected and kept as an input sample. 275 µl of the remaining cell lysates were incubated on a turning wheel for 1 h at 4°C with 8.4×10^4 Dynabeads M-270 Epoxy (Thermo Fisher Scientific) functionalized with rabbit IgG (Sigma-Aldrich). The beads were then washed thrice with 500 µl Pho-IP buffer. Bound proteins were eluted by boiling the beads for 5 min in 15 µl SDS-PAGE sample buffer, and eluates were resolved by SDS-PAGE and immunoblotted using antibodies against GFP or TAP (Thermo Fisher Scientific).

For the experiment shown in Fig. 2 E, cells were grown in 100 ml of YPD to 1 OD_{600}, collected by centrifugation at 3,500 *g* for 5 min, and resuspended in 1 ml of lysis buffer (20 mM Tris-HCl, pH 8.0, 150 mM KCl, 5 mM $MgCl_2$, and 1% Triton X-100 supplemented with 1 mM PMSF and cOmplete protease inhibitor cocktail). Cells were broken using glass beads and vortexing and then were centrifuged at 8,000 *g* for 10 min at 4°C. After centrifugation, 75 µl of the supernatant was collected and kept to represent the input (total lysate). The rest of the supernatant was incubated with 50 µl IgG Sepharose beads (GE Healthcare) prewashed with lysis buffer on a rotating wheel for 1 h at 4°C. The beads were washed once with 1 ml lysis buffer, once with lysis buffer containing 300 mM KCl, once with lysis buffer containing 500 mM KCl, once again with lysis buffer containing 300 mM KCl, and finally one more time with the lysis buffer (Reggiori et al., 2003). Bound proteins were eluted by boiling the beads for 5 min in 75 µl SDS-PAGE sample buffer, and eluates were resolved by SDS-PAGE and immunoblotted using antibodies against the myc epitope (Santa Cruz Biotechnology, Inc.) or TAP. This procedure was also used for the pulldown experiment shown in Fig. S1 A, but $MgCl_2$ was omitted form the lysis buffer.

Fluorescence microscopy

Fluorescence signals were captured at room temperature with a DeltaVision RT fluorescence microscope (Applied Precision Ltd.) equipped with a CoolSNAP HQ camera (Photometrics). Images were generated by collecting a stack of 25 pictures with focal planes 0.20 µm apart using 100× 1.49 NA objective (applying immersion oil with a 1.516 refractive index) and successive deconvolution, and then analyses were performed with SoftWoRx software (Applied Precision Ltd.). Photoshop CC and Illustrator CC software (Adobe) were used for figure preparation. A single focal plane was shown at each time.

The percentage of cells displaying Atg2-GFP and the number of Atg9 puncta per cell were determined by analyzing ≥100 cells from three independent experiments. To determine the degree of colocalization between the Atg18-GFP and mCherryV5-Atg8 fusion proteins, the number of mCherryV5-Atg8 puncta positive for the Atg18-GFP signal was also counted in ≥100 cells from three independent experiments. Subcellular positioning of the PAS was investigated by analyzing the localization of mCherryV5-Atg8 puncta in regard to ER marker proteins Sec63-GFP and vacuoles stained with CellTracker blue CMAC dye (Thermo Fisher Scientific). The mean size and intensity of the fluorescent signals of the mCherryV5-Atg8 puncta in the SEY6210 and W303 backgrounds were quantified in ≥100 cells from three independent experiments using ImageJ (National Institutes of Health).

Protein purification

Atg2–GFP-TAP, Atg2–Atg18-TAP, Atg2–$Atg18^{FAAG}$-TAP, $Atg2^{PM1}$–Atg18-TAP, and $Atg2^{PM1}$–$Atg18^{FAAG}$-TAP complexes were purified from the CUY4813, CUY9058, CUY10771, CUY10811, and CUY10813 strains, respectively. Atg9-3×FLAG was purified from the CUY10110 strain. Cells were grown at 30°C in YPG for 40 h to induce overexpression. Cells were resuspended in TAP buffer (50 mM Tris-HCl, pH 7.5, 200 mM NaCl, 1.5 mM $MgCl_2$, 1 mM DTT, and protease inhibitors) and lysed with glass beads in a FastPrep machine (MP Biomedical). For purification of Atg9, 40 mM CHAPS was added to the TAP buffer. Lysates were centrifuged at 3,000 *g* for 10 min at 4°C, and the supernatant was cleared by centrifugation at 100,000 *g* for 1 h at 4°C in an Optima L-90K ultracentrifuge using a 70 Ti rotor (Beckman Coulter). Cleared lysates were incubated with IgG Sepharose beads (GE Healthcare) or with ANTI-FLAG M2 affinity gel (Sigma-Aldrich) on a

rotary wheel for 1.5 h or 1 h, respectively, at 4°C. Bound proteins were eluted by cleavage using TEV protease at 16°C for 1 h or by adding an excess of 3×FLAG peptide for 45 min at 4°C.

Liposome and GUV preparation

Liposomes were generated by mixing 69 mol% 1,2-dioleoyl-*sn*-glycerol-3-phosphocholine (DOPC), 15 mol% 1,2-dioleoyl-*sn*-glycerol-3-phosphoethanolamine (DOPE), 12 mol% 1,2-dioleoyl-*sn*-glycerol-3-phospho-L-serine (DOPS), 0.5 mol% of the lipid dye Atto550-DPPE, and where indicated, 3 mol% PtsIns3P, in 2:1 chloroform/methanol. All lipids were purchased from Avanti Polar Lipids. The organic solvent was then evaporated, and lipids were resuspended in buffer (50 mM Tris-HCl, pH 7.5, 200 mM NaCl, 1.5 mM $MgCl_2$, and 40 mM CHAPS) to a final concentration of 2 mM. Where indicated, Atg9 was added in a 1:1,000 Atg9/lipid ratio. Liposomes were formed by detergent removal via dialysis for 16 h at 4°C and were subsequently concentrated and cleared from aggregates on a three-step Histodenz (Sigma-Aldrich) gradient by centrifugation at 100,000 *g* for 3 h at 4°C in a SW41 rotor (Beckman Coulter). Top fractions were harvested and used for the flotation assays.

GUVs were prepared using an electroformation protocol as described previously (Romanov et al., 2012). In brief, the lipid mix was dissolved in a 2:1 chloroform/methanol solution, and 3 µl was spotted onto indium tin oxide–coated slides (Nanion Technologies). The organic solvent was then evaporated under vacuum, and the slides were assembled with spacers in between them in a chamber, which was then filled with 500 µl of 300-mM sucrose. After electroformation using Vesicle Prep Pro (Nanion Technologies) over a 3-h cycle, GUVs were resuspended in the sedimentation buffer (1 mM Hepes/KOH, pH 7.4, 267 mM glucose, and 1 mM DTT) and sedimented by centrifugation at 100 *g* for 20 min at 4°C in a swing-bucket rotor (A-8-11; Eppendorf) on a sucrose cushion generated by mixing 1:1 the sedimentation buffer with the cushion buffer (1 mM Hepes/KOH, pH 7.4, 240 mM sucrose, and 1 mM DTT). GUVs were finally used within 5 h for the microscopy analyses.

Liposome flotation assay

Liposome flotation assays were conducted as the following: 20 µl liposomes were incubated with 2 µg of purified Atg2–Atg18 complex for 10 min at room temperature. The samples, which had typically of a volume of 200–300 µl, were then mixed with equal volumes of 75% sucrose in TAP buffer (final concentration, 37.5% sucrose) and successively overlaid with 25% sucrose in TAP buffer up to a final volume of 1 ml and with 200 µl TAP buffer. Gradients were centrifuged at 100,000 *g* for 1 h at room temperature in an SW41 rotor. The top fractions were collected and TCA precipitated. The proteins were resuspended in sample buffer and loaded on 7.5% SDS-PAGE gels, which finally were stained with Coomassie blue. Band intensities for Atg2, Atg9, and Atg18 were quantified using ImageJ by measuring the mean intensity within equal-sized rectangular selections. The values were inverted by subtracting them from the background (inverted or background subtracted). The intensity of the load (lane 1 in each experiment) for Atg2 and Atg18 were set to 100%, and subsequently, the relative percentages of recruitment onto liposomes for Atg2 and Atg18 for every tested condition (lanes 2–5) were calculated. To determine the ratio of the Atg9–Atg2–Atg18 complex, the intensity of Atg2 was set to 1 for every experiment and every lane before calculating the relative ratios of Atg18 and Atg9.

GUV assays and fluorescence microscopy

To monitor Atg2 binding and localization on GUVs, purified Atg2-mGFP was added at a final concentration of 100–400 pM to sedimented GUVs and incubated at room temperature in the dark for 5 min. Alternatively, purified Atg2-TAP and $Atg2^{PM1}$-TAP were incubated with twofold molar excess of DY-647 maleimide derivative (Dyomics) for 2 h at room temperature followed by removal of excess label via a NAP-5 column (GE Healthcare). GUVs were then imaged as described previously (Purushothaman et al., 2017). Atg2 binding was quantified by counting ≥50 GUVs in three independent experiments. For the maximum-intensity projections of GUVs, z stacks of 62 optical planes 0.8 µm apart were acquired with an IX-71 inverted microscope (Olympus) using a 60× 1.40 NA objective. Picture acquisition was conducted with Insight solid-state illumination and a complementary semiconductor camera (PCO) followed by deconvolution using SoftWoRx software and image processing in ImageJ and Illustrator CS4. The percentage of bound Atg2 or $Atg2^{PM1}$ was calculated by dividing the number of GUVs with bound Atg2 by the total number of counted GUVs.

Giant Ape1 assay

To produce giant Ape1 oligomers in the strains of interest, cells were transformed with pDP105 or pDP245 plasmids (Pfaffenwimmer et al., 2014). Cells were grown overnight in SMD and diluted to an early log phase the next morning. The formation of giant Ape1 oligomers was induced by addition of 250 µM $CuSO_4$ 4 h before reaching 0.6 OD_{600}, when cells were transferred into the SD-N containing 250 µM $CuSO_4$ for 1 h (Figs. 7 C, 10 A, and S2 F) or SMD containing both 400 nM rapamycin and 250 µM $CuSO_4$ for 3 h (Fig. 8, A and E; and Fig. 9 A) to induce autophagy.

IET

Yeast strains were grown in YPD medium and nitrogen starved in SD-N for 1 h before being processed for IET following the described procedure (Mari et al., 2014). Tokuyasu cryosections of 250–300-nm thickness were immunogold labeled with an anti-Ape1 antibody (Mari et al., 2010). Areas of interest were accessed by recording dual-axis tilt series with an angular range of typically −55° to +55° with 1° increments using a Tecnai 20 LaB6 transmission microscope (FEI). The recorded tilt series were aligned and processed with the IMOD software using ≥12 particles of 15-nm fiducial gold. Finally, features of interest were contoured manually in serial optical slices extracted from the tomogram and used to create surface-rendered models also using the IMOD software.

The ER proximity to the Ape1 oligomer in the generated tomograms was quantified by defining five categories of association as described in the text: *no ER*, *adjacent ER*, *tethered ER (point contact)*, *tethered ER (surface contact)*, and *tethered ER (enwrapping)*. The number of reconstructions examined for

atg2Δ (RSGY024), Atg2^{PM1}-expressing (RSGY025 and RSGY054), and Atg2^{PM4}-expressing (RSGY026 and RSGY055) cells not overexpressing Ape1 were 12, 15, and 13, respectively. The number of reconstructions examined for cells carrying giant Ape1 and Atg2 (CUY10935 transformed with the pDP105 and pYCG_YNL242w plasmids), Atg2^{PM1} (CUY10935 transformed with the pDP105 and pYCG_YNL242w_PM1 plasmids), and Atg2^{PM4} (CUY10935 transformed with the pDP105 and pYCG_YNL242w_PM4 plasmids) were 11, 9, and 9, respectively.

Morphometrical analysis of the ER

Tokuyasu cryosections of 60–80-nm thickness were stained before being randomly imaged in a transmission electron microscope (Mari et al., 2010). ER surface per cell profile was calculated using the point-hit method (Rabouille, 1999) on 16 randomly selected electron micrographs (eight with nuclear cross sections and eight without) from three different grids per condition. This method is classically used to determine the surface section of an object. In brief, the surface of the organelle of interest is determined by applying a meshing grid to the picture and counting the grip points crossing the boundaries of the organelle. The surface is then calculated by multiplying, taking in consideration the number of intersection points (P), the magnification of the picture (mag), and the space in between the meshes of the mesh grids (d) as follows: surface section (of the organelle) = $P \times d^2/mag^2$ (in μm^2).

Standard biochemical assays

Protein extraction, Western blot analyses, the GFP-Atg8 processing assay, and Pho8Δ60 activity measurement were performed as previously described (Guimaraes et al., 2015). For Western blot analyses, 2.5 OD_{600} equivalents of cells were collected by centrifugation at 13,000 *g* for 1 min and resuspended in 400 µl ice-cold 10% TCA. After leaving them on ice for ≥30 min, mixtures were centrifuged at 13,000 *g* for 5 min at 4°C, and the protein pellets were resuspended in 1 ml of ice-cold acetone by sonication. Samples were subsequently put at −20°C for ≥20 min before being centrifuged at 13,000 *g* for 5 min at 4°C. Pellets were dried, resuspended in 80–100 µl of 1× Laemmli sample buffer (50 mM Tris-HCl, pH 6.8, 2% SDS, 10% glycerol, and 1% β-mercaptoethanol), and boiled before being loaded on SDS-PAGE gels. Proteins were finally transferred on polyvinylidene difluoride membranes before being detected and quantified using an Odyssey system (Li-Cor Biosciences).

For the Pho8Δ60 assay, 5 OD_{600} equivalents of cells were lysed in 400 µl of ice-cold lysis buffer (20 mM Pipes, pH 6.8, 0.5% Triton X-100, 50 mM KCl, 100 mM potassium acetate, 10 mM $MgCl_2$, 10 µM $ZnSO_4$, and 2 mM PMSF) by vortexing in the presence of 100 µl glass beads (0.4–0.6 mm in diameter) for 3–5 min at 4°C. Lysates were centrifuged at 13,000 *g* for 5 min at 4°C. Then, 100 µl supernatant was mixed with 400 µl alkaline phosphatase reaction buffer (250 mM Tris-HCl, pH 8.5, 0.4% Triton X-100, 10 mM $MgCl_2$, 10 µM $ZnSO_4$, and 1.25 mM *p*-nitrophenyl phosphate) prewarmed at 37°C. Samples were incubated at 37°C for 20 min before adding 500 µl of 1 M glycine, pH 11.0. After centrifugation at 13,000 *g* for 2 min, the absorbance of the supernatant was measured at 400 nm.

Statistical analyses

Data represent means of three independent biological replicates ± SD. Images shown are those of a representative experiment. Data were statistically analyzed with Prism (6.0; GraphPad Software) using the paired two-tailed Student's *t* test. All comparisons with a p-value <0.05 were considered statistically significant. Nonsignificant differences are not indicated.

Online supplemental material

Fig. S1 provides evidence about the requirement of Atg9 for the stable Atg2–Atg18 interaction, but also the specificity of the BiFC signal regarding the Atg1–Atg2 interaction. Fig. S2 provides evidence that Atg2^{PM1} and Atg2^{PM4} mutants block phagophore expansion and the recruitment of Atg18 to phagophores. Fig. S3 demonstrates that the Ape1 oligomer localizes to the PAS in absence of Atg2 and in cells expressing Atg2^{PM1} or Atg2^{PM4} and reveals the presence of phagophores adjacent to the Ape1 oligomer and ER in Atg2 mutants. Fig. S4 shows that the PAS is adjacent to the ER and vacuole in Atg2^{PM1}- or Atg2^{PM4}-expressing cells. Fig. S5 highlights the relevance of Atg9 during phagophore formation. Videos 1, 2, 3, 4, 5, and 6 show 3D reconstructions with modeling of an Ape1 oligomer in the *atg2Δ* mutant with adjacent ER (Video 1), the *atg2Δ* strain with an ER tethered with a *single point of contact* (Video 2), Atg2^{PM1}-expressing cells with an ER tethered with a *surface contact* (Video 3), Atg2^{PM1}-expressing cells with an ER tethered with *enwrapping* (Video 4), and Atg2^{PM4}-expressing cells revealing the presence of a phagophore (Videos 5 and 6). Videos 7, 8, and 9 show 3D reconstructions of a giant Ape1 oligomer in Atg2^{PM1}-expressing cells with ER in close association (Video 7), Atg2^{PM4}-expressing cells with ER in close association (Video 8), and the WT strain showing the ER having a *point contact* (Video 9).

Acknowledgments

The authors thank Daniel J. Klionsky for reagents. Microscopy analyses were performed at the Microscopy and Imaging Center of the University Medical Center Groningen and at the Faculty of Science and Engineering of the University of Groningen.

F. Reggiori is supported by the Netherlands Organization for Scientific Research ALW Open Program (822.02.014), Deutsche Forschungsgemeinschaft–Netherlands Organization for Scientific Research cooperation (DN82-303), the Swiss National Science Foundation Sinergia (CRSII3_154421), the European Commission Marie Skłodowska-Curie Cofund (713660), and The Netherlands Organization for Health Research and Development VICI (016.130.606) grants. C. Ungermann is supported by the Deutsche Forschungsgemeinschaft SFB 944 (Project P11) and a grant from the Deutsche Forschungsgemeinschaft (UN111/7-3). C. Kraft is supported by a grant from the Vienna Science and Technology Fund (VRG10-001), the Austrian Science Fund (P 25522-B20 and P 28113-B28), and the European Molecular Biology Organization Young Investigators program. R. Gómez-Sánchez is supported by a European Commission Marie Skłodowska-Curie Individual Fellowship (655027).

The authors declare no competing financial interests.

Author contributions: R. Guimarães, J. Rose, R. Gómez-Sánchez, M. Mari, D. Papinski, E. Rieter, C. Kraft, C. Ungermann, and F. Reggiori conceived and designed the experiments. E. Rieter identified the Atg2 point mutants using the Y2H system. R. Guimarães, E. Rieter, and R. Hardenberg performed the Western blot analyses. R. Guimarães, J. Rose, and R. Gómez-Sánchez realized the fluorescence microscopy experiments. D. Papinski and R. Guimarães carried out the pulldown experiments. J. Rose realized the in vitro experiments. M. Mari performed the IET analyses. W.J. Geerts drew the 3D models. All authors analyzed the results. E. Rieter, R. Guimarães, J. Rose, C. Ungermann, and F. Reggiori wrote the manuscript.

Submitted: 19 October 2017
Revised: 7 March 2018
Accepted: 2 May 2018

References

Axe, E.L., S.A. Walker, M. Manifava, P. Chandra, H.L. Roderick, A. Habermann, G. Griffiths, and N.T. Ktistakis. 2008. Autophagosome formation from membrane compartments enriched in phosphatidylinositol 3-phosphate and dynamically connected to the endoplasmic reticulum. *J. Cell Biol.* 182:685–701. https://doi.org/10.1083/jcb.200803137

Bakula, D., A.J. Müller, T. Zuleger, Z. Takacs, M. Franz-Wachtel, A.K. Thost, D. Brigger, M.P. Tschan, T. Frickey, H. Robenek, et al. 2017. WIPI3 and WIPI4 β-propellers are scaffolds for LKB1-AMPK-TSC signalling circuits in the control of autophagy. *Nat. Commun.* 8:15637. https://doi.org/10.1038/ncomms15637

Barth, H., and M. Thumm. 2001. A genomic screen identifies AUT8 as a novel gene essential for autophagy in the yeast Saccharomyces cerevisiae. *Gene.* 274:151–156. https://doi.org/10.1016/S0378-1119(01)00614-X

Brachmann, C.B., A. Davies, G.J. Cost, E. Caputo, J. Li, P. Hieter, and J.D. Boeke. 1998. Designer deletion strains derived from Saccharomyces cerevisiae S288C: a useful set of strains and plasmids for PCR-mediated gene disruption and other applications. *Yeast.* 14:115–132. https://doi.org/10.1002/(SICI)1097-0061(19980130)14:2%3C115::AID-YEA204%3E3.0.CO;2-29483801

Dove, S.K., R.C. Piper, R.K. McEwen, J.W. Yu, M.C. King, D.C. Hughes, J. Thuring, A.B. Holmes, F.T. Cooke, R.H. Michell, et al. 2004. Svp1p defines a family of phosphatidylinositol 3,5-bisphosphate effectors. *EMBO J.* 23:1922–1933. https://doi.org/10.1038/sj.emboj.7600203

Finn, R.D., P. Coggill, R.Y. Eberhardt, S.R. Eddy, J. Mistry, A.L. Mitchell, S.C. Potter, M. Punta, M. Qureshi, A. Sangrador-Vegas, et al. 2016. The Pfam protein families database: towards a more sustainable future. *Nucleic Acids Res.* 44:D279–D285.

Ghaemmaghami, S., W.K. Huh, K. Bower, R.W. Howson, A. Belle, N. Dephoure, E.K. O'Shea, and J.S. Weissman. 2003. Global analysis of protein expression in yeast. *Nature.* 425:737–741. https://doi.org/10.1038/nature02046

Graef, M., J.R. Friedman, C. Graham, M. Babu, and J. Nunnari. 2013. ER exit sites are physical and functional core autophagosome biogenesis components. *Mol. Biol. Cell.* 24:2918–2931. https://doi.org/10.1091/mbc.e13-07-0381

Guan, J., P.E. Stromhaug, M.D. George, P. Habibzadegah-Tari, A. Bevan, W.A. Dunn Jr., and D.J. Klionsky. 2001. Cvt18/Gsa12 is required for cytoplasm-to-vacuole transport, pexophagy, and autophagy in *Saccharomyces cerevisiae* and *Pichia pastoris*. *Mol. Biol. Cell.* 12:3821–3838. https://doi.org/10.1091/mbc.12.12.3821

Guimaraes, R.S., E. Delorme-Axford, D.J. Klionsky, and F. Reggiori. 2015. Assays for the biochemical and ultrastructural measurement of selective and nonselective types of autophagy in the yeast Saccharomyces cerevisiae. *Methods.* 75:141–150. https://doi.org/10.1016/j.ymeth.2014.11.023

Hayashi-Nishino, M., N. Fujita, T. Noda, A. Yamaguchi, T. Yoshimori, and A. Yamamoto. 2009. A subdomain of the endoplasmic reticulum forms a cradle for autophagosome formation. *Nat. Cell Biol.* 11:1433–1437. https://doi.org/10.1038/ncb1991

He, C., M. Baba, Y. Cao, and D.J. Klionsky. 2008. Self-interaction is critical for Atg9 transport and function at the phagophore assembly site during autophagy. *Mol. Biol. Cell.* 19:5506–5516. https://doi.org/10.1091/mbc.e08-05-0544

Jain, A., and J.C.M. Holthuis. 2017. Membrane contact sites, ancient and central hubs of cellular lipid logistics. *Biochim. Biophys. Acta.* 1864:1450–1458. https://doi.org/10.1016/j.bbamcr.2017.05.017

James, P., J. Halladay, and E.A. Craig. 1996. Genomic libraries and a host strain designed for highly efficient two-hybrid selection in yeast. *Genetics.* 144:1425–1436.

Janke, C., M.M. Magiera, N. Rathfelder, C. Taxis, S. Reber, H. Maekawa, A. Moreno-Borchart, G. Doenges, E. Schwob, E. Schiebel, and M. Knop. 2004. A versatile toolbox for PCR-based tagging of yeast genes: new fluorescent proteins, more markers and promoter substitution cassettes. *Yeast.* 21:947–962. https://doi.org/10.1002/yea.1142

John Peter, A.T., B. Herrmann, D. Antunes, D. Rapaport, K.S. Dimmer, and B. Kornmann. 2017. Vps13-Mcp1 interact at vacuole-mitochondria interfaces and bypass ER-mitochondria contact sites. *J. Cell Biol.* 216:3219–3229. https://doi.org/10.1083/jcb.201610055

Juhasz, J., J.H. Davis, and F.J. Sharom. 2012. Fluorescent probe partitioning in GUVs of binary phospholipid mixtures: implications for interpreting phase behavior. *Biochim. Biophys. Acta.* 1818:19–26. https://doi.org/10.1016/j.bbamem.2011.09.006

Kaminska, J., W. Rzepnikowska, A. Polak, K. Flis, P. Soczewka, K. Bala, M. Sienko, M. Grynberg, P. Kaliszewski, A. Urbanek, et al. 2016. Phosphatidylinositol-3-phosphate regulates response of cells to proteotoxic stress. *Int. J. Biochem. Cell Biol.* 79:494–504. https://doi.org/10.1016/j.biocel.2016.08.007

Kim, J., W.-P. Huang, P.E. Stromhaug, and D.J. Klionsky. 2002. Convergence of multiple autophagy and cytoplasm to vacuole targeting components to a perivacuolar membrane compartment prior to de novo vesicle formation. *J. Biol. Chem.* 277:763–773. https://doi.org/10.1074/jbc.M109134200

Kraft, C., and S. Martens. 2012. Mechanisms and regulation of autophagosome formation. *Curr. Opin. Cell Biol.* 24:496–501. https://doi.org/10.1016/j.ceb.2012.05.001

Krick, R., J. Tolstrup, A. Appelles, S. Henke, and M. Thumm. 2006. The relevance of the phosphatidylinositolphosphat-binding motif FRR GT of Atg18 and Atg21 for the Cvt pathway and autophagy. *FEBS Lett.* 580:4632–4638. https://doi.org/10.1016/j.febslet.2006.07.041

Krick, R., S. Henke, J. Tolstrup, and M. Thumm. 2008. Dissecting the localization and function of Atg18, Atg21 and Ygr223c. *Autophagy.* 4:896–910. https://doi.org/10.4161/auto.6801

Lamb, C.A., T. Yoshimori, and S.A. Tooze. 2013. The autophagosome: origins unknown, biogenesis complex. *Nat. Rev. Mol. Cell Biol.* 14:759–774. https://doi.org/10.1038/nrm3696

Lang, A.B., A.T. John Peter, P. Walter, and B. Kornmann. 2015. ER-mitochondrial junctions can be bypassed by dominant mutations in the endosomal protein Vps13. *J. Cell Biol.* 210:883–890. https://doi.org/10.1083/jcb.201502105

Lang, T., S. Reiche, M. Straub, M. Bredschneider, and M. Thumm. 2000. Autophagy and the cvt pathway both depend on *AUT9*. *J. Bacteriol.* 182:2125–2133. https://doi.org/10.1128/JB.182.8.2125-2133.2000

Longatti, A., C.A. Lamb, M. Razi, S. Yoshimura, F.A. Barr, and S.A. Tooze. 2012. TBC1D14 regulates autophagosome formation via Rab11- and ULK1-positive recycling endosomes. *J. Cell Biol.* 197:659–675. https://doi.org/10.1083/jcb.201111079

Longtine, M.S., A. McKenzie III, D.J. Demarini, N.G. Shah, A. Wach, A. Brachat, P. Philippsen, and J.R. Pringle. 1998. Additional modules for versatile and economical PCR-based gene deletion and modification in *Saccharomyces cerevisiae*. *Yeast.* 14:953–961. https://doi.org/10.1002/(SICI)1097-0061(199807)14:10%3C953::AID-YEA293%3E3.0.CO;2-U

Lu, Q., P. Yang, X. Huang, W. Hu, B. Guo, F. Wu, L. Lin, A.L. Kovács, L. Yu, and H. Zhang. 2011. The WD40 repeat PtdIns(3)P-binding protein EPG-6 regulates progression of omegasomes to autophagosomes. *Dev. Cell.* 21:343–357. https://doi.org/10.1016/j.devcel.2011.06.024

Lynch-Day, M.A., and D.J. Klionsky. 2010. The Cvt pathway as a model for selective autophagy. *FEBS Lett.* 584:1359–1366. https://doi.org/10.1016/j.febslet.2010.02.013

Mari, M., J. Griffith, E. Rieter, L. Krishnappa, D.J. Klionsky, and F. Reggiori. 2010. An Atg9-containing compartment that functions in the early steps of autophagosome biogenesis. *J. Cell Biol.* 190:1005–1022. https://doi.org/10.1083/jcb.200912089

Mari, M., W.J. Geerts, and F. Reggiori. 2014. Immuno- and correlative light microscopy-electron tomography methods for 3D protein localization in yeast. *Traffic.* 15:1164–1178. https://doi.org/10.1111/tra.12192

Mizushima, N., T. Yoshimori, and Y. Ohsumi. 2011. The role of Atg proteins in autophagosome formation. *Annu. Rev. Cell Dev. Biol.* 27:107–132. https://doi.org/10.1146/annurev-cellbio-092910-154005

Nakatogawa, H., K. Suzuki, Y. Kamada, and Y. Ohsumi. 2009. Dynamics and diversity in autophagy mechanisms: lessons from yeast. *Nat. Rev. Mol. Cell Biol.* 10:458–467. https://doi.org/10.1038/nrm2708

Noda, T., J. Kim, W.-P. Huang, M. Baba, C. Tokunaga, Y. Ohsumi, and D.J. Klionsky. 2000. Apg9p/Cvt7p is an integral membrane protein required for transport vesicle formation in the Cvt and autophagy pathways. *J. Cell Biol.* 148:465–480. https://doi.org/10.1083/jcb.148.3.465

Obara, K., T. Sekito, K. Niimi, and Y. Ohsumi. 2008. The Atg18-Atg2 complex is recruited to autophagic membranes via phosphatidylinositol 3-phosphate and exerts an essential function. *J. Biol. Chem.* 283:23972–23980. https://doi.org/10.1074/jbc.M803180200

Ohashi, Y., and S. Munro. 2010. Membrane delivery to the yeast autophagosome from the Golgi-endosomal system. *Mol. Biol. Cell.* 21:3998–4008. https://doi.org/10.1091/mbc.e10-05-0457

Orsi, A., M. Razi, H.C. Dooley, D. Robinson, A.E. Weston, L.M. Collinson, and S.A. Tooze. 2012. Dynamic and transient interactions of Atg9 with autophagosomes, but not membrane integration, are required for autophagy. *Mol. Biol. Cell.* 23:1860–1873. https://doi.org/10.1091/mbc.e11-09-0746

Papinski, D., M. Schuschnig, W. Reiter, L. Wilhelm, C.A. Barnes, A. Maiolica, I. Hansmann, T. Pfaffenwimmer, M. Kijanska, I. Stoffel, et al. 2014. Early steps in autophagy depend on direct phosphorylation of Atg9 by the Atg1 kinase. *Mol. Cell.* 53:471–483. https://doi.org/10.1016/j.molcel.2013.12.011

Park, J.S., M.K. Thorsness, R. Policastro, L.L. McGoldrick, N.M. Hollingsworth, P.E. Thorsness, and A.M. Neiman. 2016. Yeast Vps13 promotes mitochondrial function and is localized at membrane contact sites. *Mol. Biol. Cell.* 27:2435–2449. https://doi.org/10.1091/mbc.e16-02-0112

Pfaffenwimmer, T., W. Reiter, T. Brach, V. Nogellova, D. Papinski, M. Schuschnig, C. Abert, G. Ammerer, S. Martens, and C. Kraft. 2014. Hrr25 kinase promotes selective autophagy by phosphorylating the cargo receptor Atg19. *EMBO Rep.* 15:862–870. https://doi.org/10.15252/embr.201438932

Puri, C., M. Renna, C.F. Bento, K. Moreau, and D.C. Rubinsztein. 2013. Diverse autophagosome membrane sources coalesce in recycling endosomes. *Cell.* 154:1285–1299. https://doi.org/10.1016/j.cell.2013.08.044

Purushothaman, L.K., H. Arlt, A. Kuhlee, S. Raunser, and C. Ungermann. 2017. Retromer-driven membrane tubulation separates endosomal recycling from Rab7/Ypt7-dependent fusion. *Mol. Biol. Cell.* 28:783–791. https://doi.org/10.1091/mbc.e16-08-0582

Rabouille, C. 1999. Quantitative aspects of immunogold labeling in embedded and nonembedded sections. *Methods Mol. Biol.* 117:125–144.

Rao, Y., M.G. Perna, B. Hofmann, V. Beier, and T. Wollert. 2016. The Atg1-kinase complex tethers Atg9-vesicles to initiate autophagy. *Nat. Commun.* 7:10338. https://doi.org/10.1038/ncomms10338

Reggiori, F., and C. Ungermann. 2017. Autophagosome Maturation and Fusion. *J. Mol. Biol.* 429:486–496. https://doi.org/10.1016/j.jmb.2017.01.002

Reggiori, F., C.-W. Wang, P.E. Stromhaug, T. Shintani, and D.J. Klionsky. 2003. Vps51 is part of the yeast Vps fifty-three tethering complex essential for retrograde traffic from the early endosome and Cvt vesicle completion. *J. Biol. Chem.* 278:5009–5020. https://doi.org/10.1074/jbc.M210436200

Reggiori, F., K.A. Tucker, P.E. Stromhaug, and D.J. Klionsky. 2004. The Atg1-Atg13 complex regulates Atg9 and Atg23 retrieval transport from the pre-autophagosomal structure. *Dev. Cell.* 6:79–90. https://doi.org/10.1016/S1534-5807(03)00402-7

Reggiori, F., T. Shintani, U. Nair, and D.J. Klionsky. 2005. Atg9 cycles between mitochondria and the pre-autophagosomal structure in yeasts. *Autophagy.* 1:101–109. https://doi.org/10.4161/auto.1.2.1840

Rieter, E., F. Vinke, D. Bakula, E. Cebollero, C. Ungermann, T. Proikas-Cezanne, and F. Reggiori. 2012. Atg18 function in autophagy is regulated by specific sites within its beta-propeller. *J. Cell Sci.* 126:593–604. https://doi.org/10.1242/jcs.115725

Robinson, J.S., D.J. Klionsky, L.M. Banta, and S.D. Emr. 1988. Protein sorting in Saccharomyces cerevisiae: isolation of mutants defective in the delivery and processing of multiple vacuolar hydrolases. *Mol. Cell. Biol.* 8:4936–4948. https://doi.org/10.1128/MCB.8.11.49363062374

Romanov, J., M. Walczak, I. Ibiricu, S. Schüchner, E. Ogris, C. Kraft, and S. Martens. 2012. Mechanism and functions of membrane binding by the Atg5-Atg12/Atg16 complex during autophagosome formation. *EMBO J.* 31:4304–4317. https://doi.org/10.1038/emboj.2012.278

Shintani, T., K. Suzuki, Y. Kamada, T. Noda, and Y. Ohsumi. 2001. Apg2p functions in autophagosome formation on the perivacuolar structure. *J. Biol. Chem.* 276:30452–30460. https://doi.org/10.1074/jbc.M102346200

Shintani, T., W.-P. Huang, P.E. Stromhaug, and D.J. Klionsky. 2002. Mechanism of cargo selection in the cytoplasm to vacuole targeting pathway. *Dev. Cell.* 3:825–837. https://doi.org/10.1016/S1534-5807(02)00373-8

Sikorski, R.S., and P. Hieter. 1989. A system of shuttle vectors and yeast host strains designed for efficient manipulation of DNA in *Saccharomyces cerevisiae*. *Genetics.* 122:19–27.

Sung, M.K., and W.K. Huh. 2007. Bimolecular fluorescence complementation analysis system for in vivo detection of protein-protein interaction in Saccharomyces cerevisiae. *Yeast.* 24:767–775. https://doi.org/10.1002/yea.1504

Suzuki, K., Y. Kubota, T. Sekito, and Y. Ohsumi. 2007. Hierarchy of Atg proteins in pre-autophagosomal structure organization. *Genes Cells.* 12:209–218. https://doi.org/10.1111/j.1365-2443.2007.01050.x

Suzuki, K., M. Akioka, C. Kondo-Kakuta, H. Yamamoto, and Y. Ohsumi. 2013. Fine mapping of autophagy-related proteins during autophagosome formation in Saccharomyces cerevisiae. *J. Cell Sci.* 126:2534–2544. https://doi.org/10.1242/jcs.122960

Takahashi, Y., C.L. Meyerkord, T. Hori, K. Runkle, T.E. Fox, M. Kester, T.P. Loughran, and H.G. Wang. 2011. Bif-1 regulates Atg9 trafficking by mediating the fission of Golgi membranes during autophagy. *Autophagy.* 7:61–73. https://doi.org/10.4161/auto.7.1.14015

Uemura, T., M. Yamamoto, A. Kametaka, Y.S. Sou, A. Yabashi, A. Yamada, H. Annoh, S. Kametaka, M. Komatsu, and S. Waguri. 2014. A cluster of thin tubular structures mediates transformation of the endoplasmic reticulum to autophagic isolation membrane. *Mol. Cell. Biol.* 34:1695–1706. https://doi.org/10.1128/MCB.01327-13

Velikkakath, A.K., T. Nishimura, E. Oita, N. Ishihara, and N. Mizushima. 2012. Mammalian Atg2 proteins are essential for autophagosome formation and important for regulation of size and distribution of lipid droplets. *Mol. Biol. Cell.* 23:896–909. https://doi.org/10.1091/mbc.e11-09-0785

Wang, C.-W., J. Kim, W.P. Huang, H. Abeliovich, P.E. Stromhaug, W.A. Dunn Jr., and D.J. Klionsky. 2001. Apg2 is a novel protein required for the cytoplasm to vacuole targeting, autophagy, and pexophagy pathways. *J. Biol. Chem.* 276:30442–30451. https://doi.org/10.1074/jbc.M102342200

Wittke, S., N. Lewke, S. Müller, and N. Johnsson. 1999. Probing the molecular environment of membrane proteins in vivo. *Mol. Biol. Cell.* 10:2519–2530. https://doi.org/10.1091/mbc.10.8.2519

Yamamoto, H., S. Kakuta, T.M. Watanabe, A. Kitamura, T. Sekito, C. Kondo-Kakuta, R. Ichikawa, M. Kinjo, and Y. Ohsumi. 2012. Atg9 vesicles are an important membrane source during early steps of autophagosome formation. *J. Cell Biol.* 198:219–233. https://doi.org/10.1083/jcb.201202061

Yamamoto, H., Y. Fujioka, S.W. Suzuki, D. Noshiro, H. Suzuki, C. Kondo-Kakuta, Y. Kimura, H. Hirano, T. Ando, N.N. Noda, and Y. Ohsumi. 2016. The Intrinsically Disordered Protein Atg13 Mediates Supramolecular Assembly of Autophagy Initiation Complexes. *Dev. Cell.* 38:86–99. https://doi.org/10.1016/j.devcel.2016.06.015

Ylä-Anttila, P., H. Vihinen, E. Jokitalo, and E.L. Eskelinen. 2009. 3D tomography reveals connections between the phagophore and endoplasmic reticulum. *Autophagy.* 5:1180–1185. https://doi.org/10.4161/auto.5.8.10274

Young, A.R.J., E.Y.W. Chan, X.W. Hu, R. Köchl, S.G. Crawshaw, S. High, D.W. Hailey, J. Lippincott-Schwartz, and S.A. Tooze. 2006. Starvation and ULK1-dependent cycling of mammalian Atg9 between the TGN and endosomes. *J. Cell Sci.* 119:3888–3900. https://doi.org/10.1242/jcs.03172

Zheng, J.X., Y. Li, Y.H. Ding, J.J. Liu, M.J. Zhang, M.Q. Dong, H.W. Wang, and L. Yu. 2017. Architecture of the ATG2B-WDR45 complex and an aromatic Y/HF motif crucial for complex formation. *Autophagy.* 13:1870–1883. https://doi.org/10.1080/15548627.2017.1359381